# OPTIMIZATION ALGORITHMS IN COMPRESSIVE SENSING (CS) SPARSE MAGNETIC RESONANCE IMAGING (MRI)

By

Viliyana Takeva - Velkova

Faculty of Science, University of Ontario Institute of Technology

June, 2010

# Abstract

Magnetic Resonance Imaging (MRI) is an essential instrument in clinical diagnosis; however, it is burdened by a slow data acquisition process due to physical limitations. Compressive Sensing (CS) is a recently developed mathematical framework that offers significant benefits in MRI image speed by reducing the amount of acquired data without degrading the image quality. The process of image reconstruction involves solving a nonlinear constrained optimization problem. The reduction of reconstruction time in MRI is of significant benefit.

We reformulate sparse MRI reconstruction as a Second Order Cone Program (SOCP). We also explore two alternative techniques to solving the SOCP problem directly: NESTA and specifically designed SOCP-LB.

# Acknowledgements

> " . . . each day is a journey and the journey itself home."
>
> Matsuo Basho

I would like to thank my husband and son who have unconditionally put their lives on hold and have patiently waited for my return home.

I would like to thank my supervisor Dr. Dhavide Aruliah who has guided me wisely and has lent me more than a big helping hand in taking the most of this journey and finally finding my way home.

# Author's Declaration

I declare that this work was carried out in accordance with the regulations of the University of Ontario Institute of Technology. The work is original except where indicated by special reference in the text and no part of this document has been submitted for any other degree. Any views expressed in the dissertation are those of the author and in no way represent those of the University of Ontario Institute of Technology. This document has not been presented to any other University for examination either in Canada or overseas.

_____

Viliyana Takeva - Velkova

Date: June 30, 2010

# Contents

# Contents

# List of Tables

# List of Figures

# Chapter 1

# Introduction

MRI as a comparatively new medical imaging tool gains popularity and is preferred in the field of clinical diagnosis for two reasons. It increases the quality of the acquired image. At the same time, it reduces the imaging time. Obtaining a qualitative image quickly is crucial in a wide range of clinical applications: dynamic heart, functional brain, angiography, etc.

In search of a balanced and reasonable tradeoff between the above mentioned requirements for quality and speed, MRI practitioners have improved the hardware to reduce scan time by developing fast pulse sequences and efficient scanning trajectories. The impressive gains in reducing data acquisition time that way have reached their potential. The reason is in some fundamental technical and physiological limitations associated with rapidly switched magnetic field gradients.

These limitations drive researchers to seek other methods for increasing the speed of data acquisition while preserving image quality. Thus, reducing the amount of the collected data arises as another possibility of fast data acquisition. Parallel MRI (pMRI) is one example of a hardware implementation for improving MRI performance [21, 22]; it resolves the issue of slow acquisition by exploiting redundancy in k-space (the domain in which data is sampled).

More specifically, pMRI undersamples uniformly phase encoded lines in **k**-space during the image acquisition. Data collected from several coils with distinct spatial sensitivities is used in the reconstruction process.

Recently, a mathematical framework called compressive sensing (CS) has emerged. It allows reducing the amount of acquired data by randomly undersampling the measurements without compromising the image quality. MRI systems naturally encode the images by measuring Fourier coefficients rather than pixels. They also meet the CS requirement for compressibility of the images in a transform domain. Hence, MRI has the potential to benefit from the CS theory, provided an appropriate reconstruction algorithm can be designed to recover the image.

The contributions of this thesis are in studying alternative optimization algorithms for solving the CS sparse MRI reconstruction problem. The first contribution is in reformulating the complex-value problem as an equivalent real-value Second Order Cone Program (SOCP). Another contribution is in exploring and presenting the excellent performance of two alternative techniques to solving directly the SOCP problem: SOCP-LB and NESTA. The SOCP-LB solver uses log-barrier method and we specifically designed it to handle the complex input data. NESTA is a competitive publicly released $1^{st}$-order solver developed by Becker and Candes [16]. Its reliability for solving compressed sensing MRI recovery problems is confirmed in our experiments.

## 1.1 Thesis Outline

Chapter 2 of this thesis is an overview of the MRI theory. It introduces key terms and principles underlying the fundamentals of nuclear magnetic resonance (NMR). In addition, it gives an idea of the imaging process through describing the signal detection, signal encoding, and image acquisition processes.

In Chapter 3 we review the basic CS concepts. We start by comparing and contrasting the traditional approach with the CS approach to sampling an object. Next, we introduce an experiment which motivates the CS development, followed by more detailed description of the CS central concept. The end of the chapter clarifies how MRI is a natural fit to a CS system.

Chapter 4 goes to the core work of this project. After briefly covering convex optimization terminology, the chapter formulates the SOCP for a sparse MRI reconstruction and introduces the theory of two algorithms for solving the formulation: SOCP-LB and NESTA. These are the solvers with which the experiments are run. In Chapter 5 we establish the experimental protocol and describe the results from the numerical experiments. Finally, in Chapter 6 we summarize the benefits of our project to the clinical MRI and point to some possible future work developments.

## 1.2 Notations

For clarity, we provide a summary of the notations used for the rest of the thesis. Vectors in all chapters are written in lower case boldfaced letters. Some exceptions apply for Chapter 2 where some vectors are denoted by capital boldfaced letters. All matrices are written in capital letters unless otherwise specified. $\mathbb{R}$ represents the set of real numbers and $\mathbb{C}$ represents the set of complex numbers.

We also introduce some standard terminology used in the discussion throughout.

## 1.2.1 Vector Norms

**Definition 1.** The $\ell_2$-norm of a vector $\mathbf{x} \in \mathbb{R}^N$ (or $\mathbb{C}^N$) is defined by

$$\|\mathbf{x}\|_2 = \left[ \sum_{i=1}^{N} |x_i|^2 \right]^{\frac{1}{2}} \tag{1.2.1}$$

**Definition 2.** The $\ell_1$-norm of a vector $\mathbf{x} \in \mathbb{R}^N$ (or $\mathbb{C}^N$) is defined by

$$\|\mathbf{x}\|_1 = \sum_{i=1}^{N} |x_i| \tag{1.2.2}$$

**Definition 3.** Total variation (TV) of an image. Let $x_{ij}$ be the element in the $i^{th}$ row and $j^{th}$ column of a two-dimensional object $X \in \mathbb{R}^{n \times n}$. Define the horizontal and vertical differences as follows

$$
\begin{aligned}
D_{h;ij}X &= \begin{cases} x_{i+1,j} - x_{ij} & \text{if } i < n \\ 0 & \text{if } i = n \end{cases} \\
D_{v;ij}X &= \begin{cases} x_{i,j+1} - x_{ij} & \text{if } j < n \\ 0 & \text{if } j = n. \end{cases}
\end{aligned}
\tag{1.2.3}
$$

Then, the total variation of $X$ is defined to be

$$\|X\|_{TV} := \sum_{ij} \|\nabla x_{ij}\|_2, \quad \nabla x_{ij} = [D_{h;ij}X, D_{v;ij}X]^T. \tag{1.2.4}$$

Observe that the total variation of $X$ is not actually a norm in the usual sense, but, in keeping with the established trend in the literature, we use the notation $\|X\|_{TV}$.

**Definition 4.** The $\ell_0$-norm of a vector $\mathbf{x} \in \mathbb{R}^N$ (or $\mathbb{C}^N$) is defined by

$$\|\mathbf{x}\|_0 := \text{number of nonzero entries in } \mathbf{x}. \tag{1.2.5}$$

Observe that the mapping defined in (1.2.5) is not actually a vector norm in spite of the fact that this notation has become common in the compressed sensing literature.

## 1.2.2 Fourier Transform

**Definition 5.** The *Fourier transform* for a continuous function $f(x)$ is defined by

$$f(\omega) = \int_{-\infty}^{+\infty} f(x)e^{-i\omega x}dx \qquad (1.2.6)$$

with $\omega \in \mathbb{R}$.

For an $N$-periodic discrete function $f$, the integral in (1.2.6) is replaced by a sum, changing the expression to

$$\sum_{k=0}^{N-1} f_k e^{-i\omega k}. \qquad (1.2.7)$$

Considering $\omega$ of the form $\omega_j = 2\pi j/N$, for each choice of $k$, $e^{-i\omega_j k} = e^{-i2\pi kj/N}$ is $N$-periodic in the $j$ variable just as $f_k$ is periodic in the $k$ variable. That way, the Fourier transform of the discrete function $f_k$ is also a discrete function and is defined in (1.2.8) below [19].

**Definition 6.** The *discrete Fourier transform*, denoted by $\mathfrak{F}_D$, transforms an $N$-periodic discrete function $f$ into another discrete function $\mathfrak{F}_D f$ defined by

$$(\mathfrak{F}_D f)_j = \sum_{k=0}^{N-1} f_k e^{-i2\pi kj/N} \quad \text{for} \quad j = 0, 1, \ldots, (N-1). \qquad (1.2.8)$$

# Chapter 2

# Introduction to MRI

Even though magnetic resonance imaging (MRI) was developed relatively recently, it is based on a technology that dates back over half a century. The study of nuclear magnetic resonance (NMR) began in 1946 with the (independent) experiments of Edward Purcell at Harvard and Felix Bloch at Stanford. NMR provides the foundation for NMR spectroscopy which has proved to be an invaluable tool in many scientific disciplines. Over the last thirty years, radiology has been revolutionized by the application of NMR to imaging, commonly known as magnetic resonance imaging.

## 2.1 Fundamentals of Nuclear Magnetic Resonance (NMR)

### 2.1.1 Spin System Magnetization

Nuclear magnetic resonance can be described as the response of magnetic nuclei in a uniform magnetic field to radio frequency magnetic field (tuned through resonance). Magnetic resonance can occur in systems with constituents having two main properties:

- magnetic moment $\mu$

- spin $\mathbf{J}$ (also called angular momentum) .

An example of nuclei with nonzero $\mathbf{J}$ and $\mu$, which happen to be of common interest in MRI, are those of hydrogen atoms. They are most abundant in the water and fat molecules in our body. In its classical interpretation, a nucleus is viewed as a spinning charged object and is expected to develop a magnetic field due to its net charge. In quantum mechanics, the intrinsic spin of each nucleon further adds to the magnetic field of the nucleus.It is specifically this magnetic field referred to as its magnetic moment $\mu$. The two main properties are related by

$$\mu = \gamma \mathbf{J}, \tag{2.1.1}$$

where $\gamma$ is the *gyromagnetic ratio* which is constant for a given nucleus in its ground state. All nuclei of the same type that are present in an object constitute a spin system with bulk magnetization $\mathbf{M}$, a vector sum of the magnetic moments in the system, expressed as

$$\mathbf{M} = \mathbf{M_{xy}} + \mathbf{M_z} \tag{2.1.2}$$

where $\mathbf{M_z}$ is referred to as its longitudinal magnetization component and $\mathbf{M_{xy}}$ is referred to as its transverse magnetization component with

$$\mathbf{M_{xy}} = \mathbf{M_x} + \mathbf{M_y}. \tag{2.1.3}$$

The three components of the bulk magnetization $\mathbf{M}$ can be expressed as

$$\mathbf{M_x} = M_x \mathbf{i}, \tag{2.1.4}$$

$$\mathbf{M_y} = M_y \mathbf{j}, \quad \text{and} \tag{2.1.5}$$

$$\mathbf{M_z} = M_z \mathbf{k}. \tag{2.1.6}$$

## 2.1.2 Net Magnetization and $B_0$ Field

The orientation of the magnetic dipoles in a generic spin system is random, so the bulk magnetization $\mathbf{M} \equiv \mathbf{0}$. In a typical MR imager, a strong external magnetic field $\mathbf{B_0}$ is imposed by a large solenoidal coil. The field $\mathbf{B_0}$ is approximately $1.5\,\mathrm{T}$ which is about ten thousand times larger than the magnetic field of the earth. By convention, the $z$-axis is chosen parallel to the direction of the external field $\mathbf{B_0}$ and the object being imaged is also aligned with this axis (i.e., for a person in an MR imager, the $z$-axis increases traveling from the toes toward the head).

The effect of the field $\mathbf{B_0}$ inside an MR imager is to polarize the protons of the system being scanned. That is, the bulk magnetization $\mathbf{M}$ of the object inside the field aligns with the external field. Each microscopic magnetic dipole precesses about the $z$-axis with random phase. As the phases of the individual dipoles are random, the component of the bulk magnetization perpendicular to the imposed field vanishes, i.e., $\mathbf{M_{xy}} = \mathbf{0}$. More specifically, $M_x = M_y = 0$. On the other hand, inside the imager and at equilibrium we find $M_z \neq 0$. Thus, the effect of the field $\mathbf{B_0}$ is to create a preferred orientation of the magnetic dipoles within the imager.

Therefore, by applying the external magnetic field $\mathbf{B_0}$, the net magnetization is realigned to point in the positive $z$ direction, i.e., at equilibrium,

$$\mathbf{M} = M_z \mathbf{k} \tag{2.1.7}$$

holds. Moreover, there is a quantitative relationship between the frequency of precession $\omega_0$ of the magnetic dipoles that is induced by the field $\mathbf{B_0}$ and the field strength $B_0 = \|\mathbf{B_0}\|$, namely

$$\omega_0 = \gamma B_0. \tag{2.1.8}$$

The quantity $\omega_0$ in (2.1.8) is known as the *Larmor frequency* associated with the field strength $B_0$. The gyromagnetic ratio, also in (2.1.2) depends on the

kind of atoms in the field; for a hydrogen atom, $\gamma = 42.58\,\text{MHz/T}$, so, given a field $B_0 = 1.5\,\text{T}$, the Larmor frequency of hydrogen atoms in this field is $\omega_0 \simeq 64\,\text{MHz}$.

### 2.1.3   Net Magnetization and $\mathbf{B_1}$ Field

Detecting an image requires phase coherence (i.e., resonance) in the system of precessing magnetic moments. To attain phase coherence, an external force is applied to the system (which, at equilibrium, is already oscillating at frequency $\omega_0$). The external forcing takes the form of an oscillating magnetic field denoted $\mathbf{B_1}$. The field $\mathbf{B_1}$ is referred to as an *RF pulse* for two principle reasons:

1. The field oscillates near the Larmor frequency of hydrogen which is in the radio frequency band; and

2. The field is applied for a short period of time (typically microseconds or milliseconds).

Most commonly, an RF pulse is given by [1]

$$\mathbf{B_1}(t) = 2B_1^e(t) \cos\left(\omega_{rf} t + \varphi\right) \mathbf{i}, \tag{2.1.9}$$

where the parameters defining the RF pulse are

- $B_1^e(\text{t})$, the envelope function;

- $\omega_{rf}$, the excitation carrier frequency; and

- $\varphi$, the initial phase angle.

Given a spin system at equilibrium inside an externally imposed uniform magnetic field $\mathbf{B_0}$, the effect of the RF pulse is to tip the bulk magnetization $\mathbf{M}$ away from the $z$-axis. That is, introducing the field $\mathbf{B_1}$ tips the bulk magnetization $\mathbf{M}$ out of alignment with the external field producing a nonzero transverse component $\mathbf{M_{xy}} \neq \mathbf{0}$.

### 2.1.4  Excitation Governing Law

The spin system is excited with the net magnetization vector disturbed from its thermal equilibrium as a result of applying an RF pulse. The time evolution of the bulk magnetization in response to the excitation by the RF pulse is governed by the Bloch equation [1]

$$\frac{d\mathbf{M}}{dt} = \gamma \mathbf{M} \times \mathbf{B} - \frac{M_x \mathbf{i} + M_y \mathbf{j}}{T_2} - \frac{(M_z - M_z^0)\,\mathbf{k}}{T_1}, \tag{2.1.10}$$

where $M_z^0 \mathbf{k}$ is the magnetization at thermal equilibrium, $\gamma$ is the gyromagnetic ratio, $T_1$ and $T_2$ are times scales characterizing the amount of time required for the spin system to return to thermal equilibrium after the RF pulse ceases. As with the gyromagnetic ratio $\gamma$, the time constants $T_1$ and $T_2$ are material-dependent properties that are different for distinct types of matter.

### 2.1.5  Relaxation

After the duration of the RF pulse, the perturbed magnetized spin system returns to thermal equilibrium. This process is called *relaxation* and is characterized by the longitudinal and transverse components of the magnetization, denoted respectively as $M_z \mathbf{k}$ and $\mathbf{M_{xy}}$. Equations for these two components are obtained by solving the Bloch equation for $\mathbf{B_1} = \mathbf{0}$. Both magnetization components change exponentially with time, i.e.,

$$M_{xy}(t) = M_{xy}(0^+)e^{-t/T_2} \tag{2.1.11}$$

$$M_z(t) = M_z^0(1 - e^{-t/T_1}) + M_z(0^+)e^{-t/T_2} \tag{2.1.12}$$

where $M_{xy}(0^+)$ and $M_z(0^+)$ are the magnitudes of $\mathbf{M_{xy}}(t)$ and $M_z \mathbf{k}(t)$ respectively after excitation by the RF pulse. $T_1$ is the relaxation time for which the longitudinal magnetization recovers to the thermal equilibrium value it had before the action of RF pulse. $T_2$ is the relaxation time for which the transverse magnetization dies out (Figure 2.1). Transverse relaxation is more rapid

compared to the longitudinal relaxation, i.e., $T_2 \leq T_1$. Typically, $T_1$ is in the range $300 - 2000$ ms opposed to $30 - 150$ ms for $T_2$.
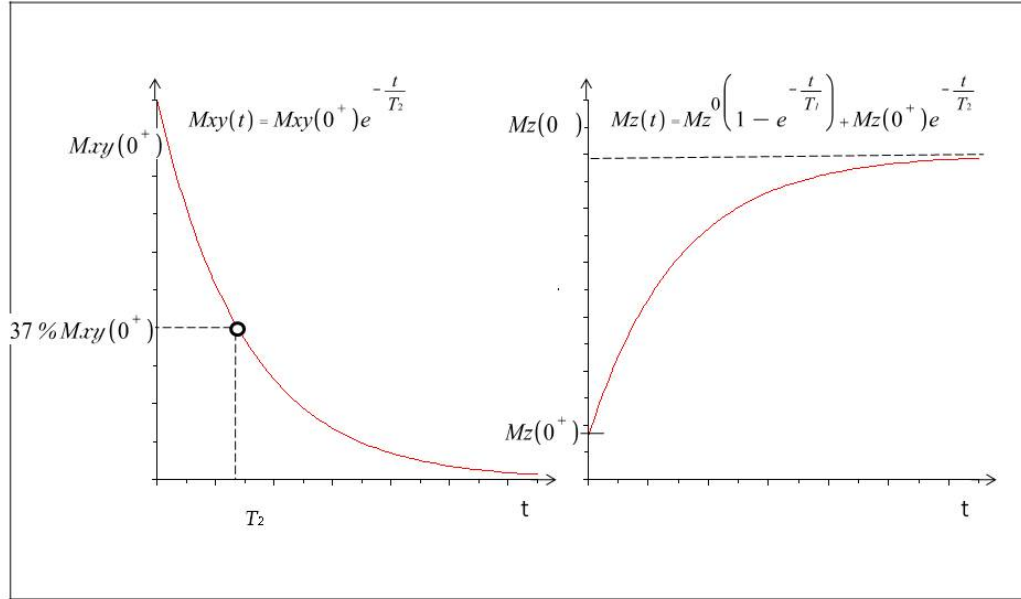


Figure 2.1: Relaxation curves of transverse and longitudinal magnetization during the process of relaxation.

## 2.2 Imaging

### 2.2.1 Signal Spatial Encoding

Each location $\mathbf{r} = x\,\mathbf{i} + y\,\mathbf{j} + z\,\mathbf{k}$ in the imaged object produces an identical signal provided only the homogeneous effects of $\mathbf{B_0}$ and $\mathbf{B_1}$ are present in the body. The signal consists of photons that are emitted by the nuclei which change their quantum state during relaxation. The time-varying signal $V(t)$ induced in the receiver coil under only the effect of these fields cannot distinguish the individual signal contributions from these locations. Therefore, the task of

determining a spatial image seems hopeless. To eliminate this difficulty, the fields are supplemented with auxiliary magnetic fields created by three gradient coils. Applying the gradient field $\mathbf{G}(t)$ introduces spatial variation into the Larmor frequency. That is, the Larmor frequency $\omega(\mathbf{r})$ varies proportionally to the gradient field

$$\omega(\mathbf{r}) = \gamma(\mathbf{B_0} + \mathbf{G}(t) \cdot \mathbf{r}) \qquad (2.2.1)$$

where $\mathbf{G}(t)$ is a magnetic field gradient (or gradient field) and $\mathbf{r}$ is the spatial position.

The expression in (2.2.1) defines a spatially varying Larmor frequency. Consider $\omega = 2\pi f$ added by the gradient fields can be expressed as [2]

$$f(\mathbf{r}) = \frac{\gamma}{2\pi} \mathbf{G}(t) \cdot \mathbf{r}. \qquad (2.2.2)$$

Integrating the frequency over the time of the RF pulse defines the *phase of magnetization*

$$\phi(\mathbf{r}, t) = 2\pi \int_0^t \frac{\gamma}{2\pi} \mathbf{G}(s) \cdot \mathbf{r} ds \qquad (2.2.3)$$

and the *spatial frequency*

$$\mathbf{k}(t) = \frac{\gamma}{2\pi} \int_0^t \mathbf{G}(s) ds. \qquad (2.2.4)$$

Thus,

$$\phi(\mathbf{r}, t) = 2\pi \mathbf{r} \cdot \mathbf{k}(t). \qquad (2.2.5)$$

In the entire volume, the measured signal is

$$s(t) = \int_{\mathbb{R}^3} m(\mathbf{r}) e^{-i2\pi \mathbf{k}(t) \cdot \mathbf{r}} d\mathbf{r}, \qquad (2.2.6)$$

where the scalar field $m(\mathbf{r})$ is the magnitude of the bulk magnetization at position $\mathbf{r}$, i.e., $m(\mathbf{r}) = \|\mathbf{M}(\mathbf{r})\|$. Equation (2.2.6) is the *signal equation* for MRI. It demonstrates that the signal encodes the spatial position $\mathbf{r}$ and the magnetization strength $m(\mathbf{r})$ at those positions. In other words, the signal equation reveals that the received signal $s(t)$ at time $t$ is the Fourier transform of the object of interest $m(\mathbf{r})$ sampled at spatial frequency $\mathbf{k}(t)$.

The RF field together with the gradients can be tuned in a way that selectively limits the magnetization excitation to a particular spatial slice. The frequency of the RF field is adjusted to be close to the resonance frequency of the slice. The imaging spatial encoding in this case is two-dimensional. The RF field and gradients can also be tuned to select a volume, in which case the imaging spatial encoding is three-dimensional.

### 2.2.2 Signal Detection

The precession of magnetization $\mathbf{M_{xy}}$ generates a measurable signal. The time-varying magnetic flux (related to the magnetic field in the plane of the receiver coil) induces a changing voltage in a receiver coil tuned to the resonance frequency. In MRI, depending on the stage of the signal detection module, the observed signal can be referred to as the *transverse magnetization* or the *induced voltage signal*.

The transverse magnetization, which is time-dependent and position dependent, is represented in complex form by

$$M_{xy}(\mathbf{r}, t) = M_{xy}(0^+)e^{-i\omega_{rf}t}, \qquad (2.2.7)$$

where $M_{xy}(0^+)$ is the magnitude of the transverse magnetization after excitation by an RF pulse and $\omega_{rf}t$ is the corresponding phase at time $t$.

Assuming the receiver coil is stationary and the receiver sensitivity is uniform over the region of interest, the voltage signal $V(t)$ induced in the receiver coil is given by

$$V(t) = \int_{\text{body}} M_{xy}(\mathbf{r}, 0)e^{-i\Delta\omega_{rf}t}\, d\mathbf{r}, \qquad (2.2.8)$$

where $\Delta\omega_{rf}$ is the difference between the Larmor frequency at position $\mathbf{r}$ associated with the magnetic field $\mathbf{B_0}$ of the main magnet and frequency of $\omega_{rf}$ of the RF pulse.

### 2.2.3 Image Acquisition

The essence of image acquisition is the collection of a series of frames of data. For each frame a new transverse magnetization is created and sampled. The number of samples that can be acquired is physically constrained by a number of factors amongst which is a limited data acquisition time. Those limitations in time are due to exponentially decaying transverse magnetization, limited gradient performance, and physiological constraints. Therefore, it is only possible to sample a portion of **k**-space in each data acquisition. For the reconstruction of one MR image, a sufficient number of acquisitions is required. Image reconstruction is based on data from all acquisitions. Parameters tailored to and characterizing the image acquisition process are the *pulse sequence, k-space trajectories,* and *field of view (FOV).*

### 2.2.4 Pulse Sequence

The selection of the gradient waveforms $\mathbf{G}(t)$ together with the RF pulse $\mathbf{B_1}(t)$ constitutes the *pulse sequence* that produces the MRI signal. A simplified example of a pulse sequence is shown on a *pulse-timing diagram* (See Figure 2.2). It contains a 90° slice selective $RF$ pulse, a slice selection gradient pulse $\mathbf{G_z}$, a phase-encoding gradient pulse $\mathbf{G_y}$, a frequency-encoding gradient pulse $\mathbf{G}_x$, and a measured signal. First, a 90° RF pulse is turned on in the presence of a slice selection gradient, selectively exciting the slice of interest. A phase-encoding gradient is turned on once the RF pulse is complete and the slice selection gradient is turned off. Next, after the phase-encoding gradient has been turned off, a frequency-encoding gradient is turned on and a signal is recorded. This sequence of pulses is usually repeated 128 or 256 times to collect all the data needed to produce an image.
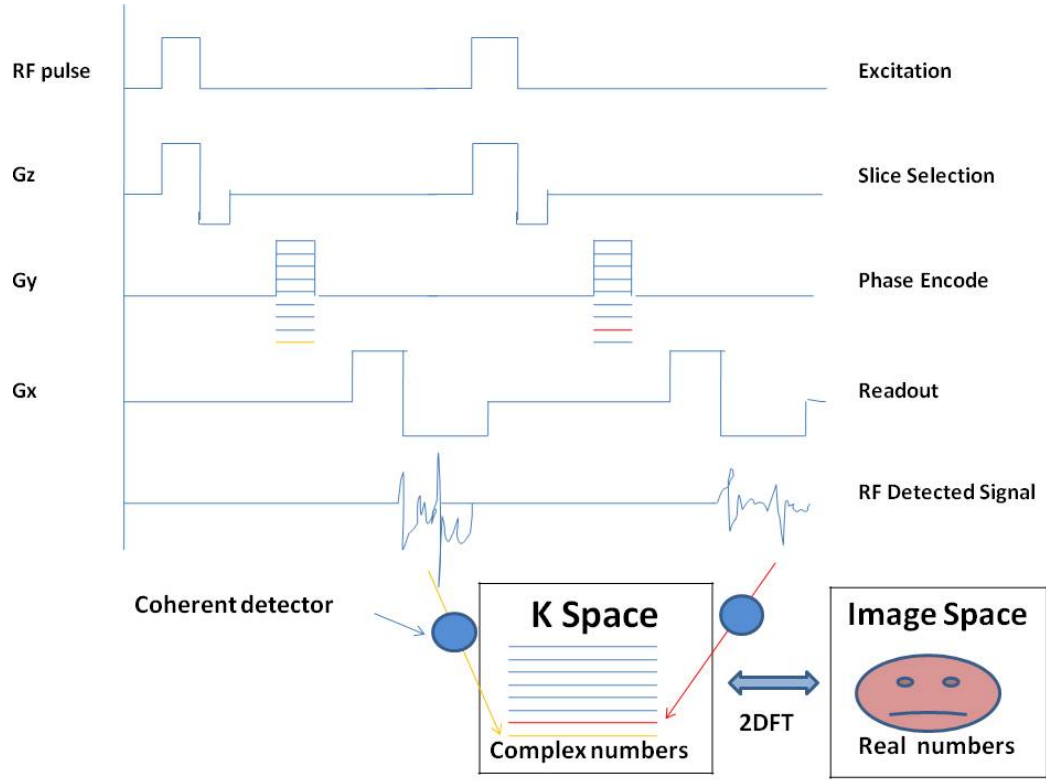
Figure 2.2: Pulse timing diagram of a simplified pulse sequence.

## 2.2.5 K-space Trajectories

The integral of the gradient waveforms traces out a trajectory of $\mathbf{k}(t)$ in the spatial frequency space. Some common trajectories used in the MRI data acquisition process are Cartesian, radial, spirals (See Figure 2.3). There are a variety of shapes available for $\mathbf{k}$-space trajectories that have advantages in different application-specific contexts. Cartesian trajectories are widespread in clinical MRI because reconstructing an image from data sampled along Cartesian paths is simple and robust to various types of perturbations. Spirals are preferred trajectories in real-time and rapid imaging applications. High contrast objects can be imaged using radial trajectories; radial trajectories are useful because they allow significant undersampling of $\mathbf{k}$-space and are less susceptible to motion artifacts than certain other trajectories [2].

Imaging time is proportional to the number of data points acquired in $\mathbf{k}$-space.

Recall the pulse timing diagram above: for each sampled line acquired, the frequency gradients are identical while the phase-encoding gradient changes. As mentioned earlier, tracing each acquired phase-encoded line requires a sequence of pulses which affects the acquisition time. In the chapters to follow I will introduce and review the theory of methods to work with fewer acquisitions.



(a) Cartesian          (b) Spiral          (c) Radial
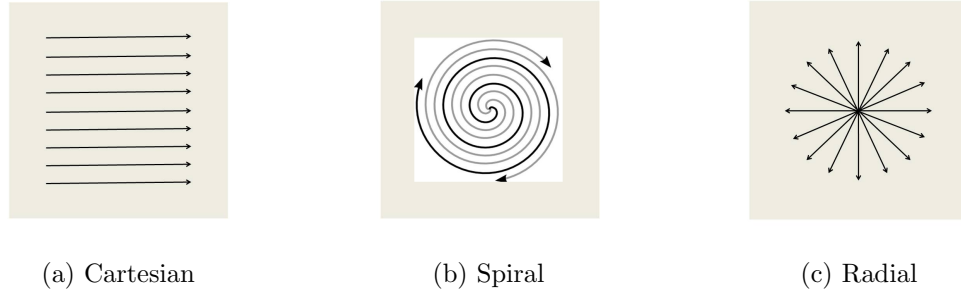
Figure 2.3: Examples of sampling trajectories.
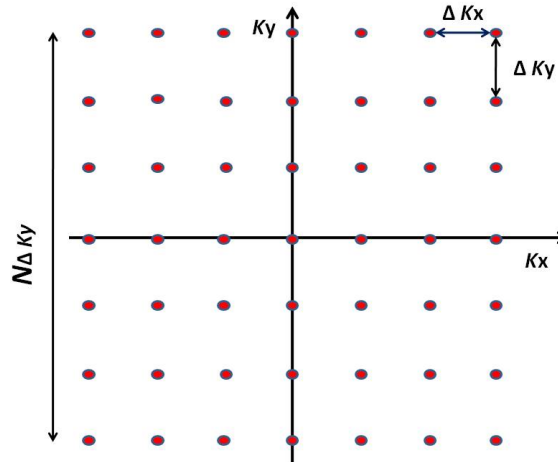


Figure 2.4: Cartesian sampling of **k**-space with related characteristics.

## 2.2.6  Field of View

**k**-space is discretely sampled; therefore, some terms related to the Discrete Fourier Transform need to be specified. That will bring clarity to our discussion in Chapter 3 on how the reconstruction requirements are met, provided that

the Nyquist criterion is applied. The Nyquist criterion is described in the Shannon-Nyquist sampling theorem. Its original statement (1949) reads, "If a function $x(t)$ contains no frequencies higher than $B$ Hz, it is completely determined by giving its ordinates at a series of points spaced $1/(2B)$ seconds apart"

A *pixel* is the smallest spatial unit that can be resolved in an image. In the case of Cartesian sampled **k**-space with $N$ points, $\Delta k_y$ spaced from each other, the pixel size is

$$\Delta y = \frac{1}{N \Delta k_y}. \tag{2.2.9}$$

*Field of view (FOV)* in MRI determines the size of the image, i.e., it is the largest area that can be reconstructed from the sampled data without violating the conditions in Nyquist theorem:

$$\Delta k_x \le \frac{1}{W_x} \qquad\qquad \Delta k_y \le \frac{1}{W_y}, \tag{2.2.10}$$

where $W_x$ and $W_y$ are the widths of the resulting image space. If the FOV is not large enough to encompass the reconstructed image, problems like aliasing and artifacts might occur in it [1]. The FOV is proportional to the sampling density in the sampled area.

*Image resolution* is determined by the sampled area of **k**-space and is proportional to its size. The denser the sampling, the higher the image resolution is.

As previously mentioned, the sampling density along the phase-encoded direction, $k_y$, imposes a lower limit on the scan time. In other words, if a way can be found to reduce the sampling density, reduction in scan time will be achieved. Fortunately, algorithms implementing the revolutionary Compressive Sensing theory have been developed to allow image recovery below Nyquist rate without degrading its quality. In the next chapters, after introducing the principles of CS theory, we present algorithms effectively implementing it.

# Chapter 3

# Compressive Sensing (CS)

## 3.1 Classical vs CS Approach to Sampling Objects

The idea of Compressive Sensing (CS) was presented in 2006 by E.J. Candes, J. Romberg, and T. Tao and D. Donoho in their original works [8] and [4] , respectively. The main principle underlying the traditional signal acquisition is the Shannon-Nyquist sampling theorem: "the sampling rate must be at least twice the maximum frequency present in the signal (the so-called Nyquist rate)" [7]. A typical sampling device is constructed to observe Shannon-Nyquist's criterion. Related to this device is a typical data acquisition process which undergoes two main stages (Figure 3.1):

1. Sampling (densely and uniformly): massive amounts of data are collected. In mathematical language, coefficients of the acquired signal are computed to form the complete data set.

2. Compression: Large part of the gathered information is discarded to facilitate storage and transmission, i.e., the largest coefficients are coded and the remaining ones are thrown away. Thus, high-resolution signals

are converted into small bit streams.

The shortcoming of this traditional data acquisition process is in the waste it brings in terms of time and resources involved. Logically, one can ask "Is there a way to avoid this waste?" As expected, the answer is yes, and that is basically what CS is all about.

The CS paradigm appears to contradict the common rule of sampling at Nyquist rate. It postulates that under certain conditions, one can accurately recover signals and images from considerably fewer measurements compared to the measurements required by traditional Nyquist sampling. In the CS concept, the data acquisition and compression processes are squeezed into one single step by acquiring only the encoded largest coefficients of the image directly into the acquisition (See Figure 3.2). Thus, the shortcoming of the classical approach is eliminated.
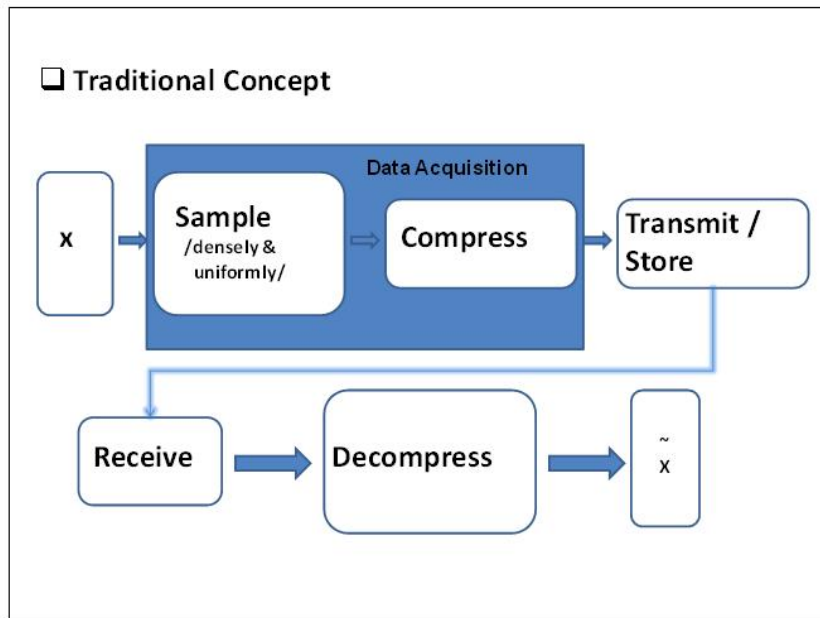
Figure 3.1: The imaging process using traditional data acquisition concept.
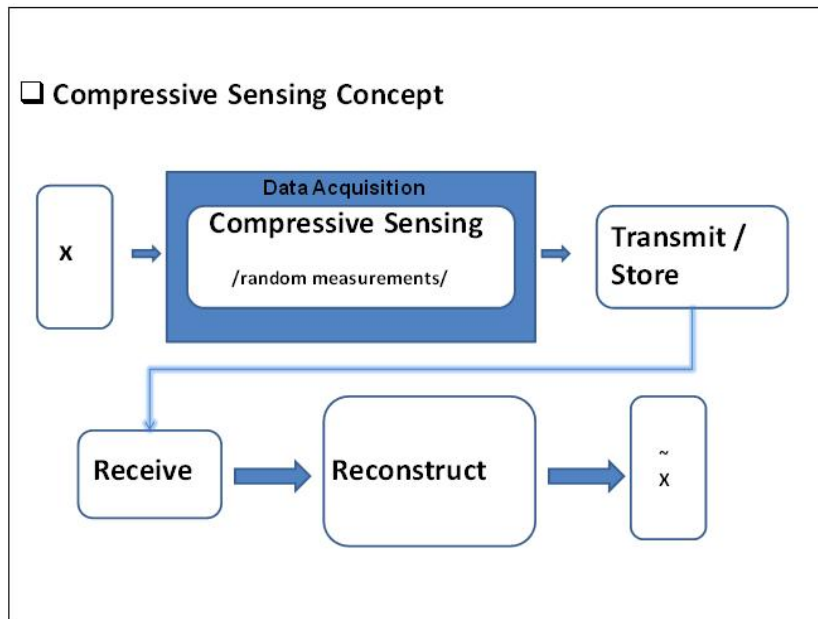
Figure 3.2: The imaging process using CS data acquisition concept.

## 3.2   Experiment by Candés, Romberg, and Tao

While undersampling significantly improves data acquisition speed, reconstruction from samples gathered that way is challenging. Standard signal reconstructions using Fourier techniques that violate the Nyquist criterion result in aliasing artifacts [4]. Figure 3.3a shows the original image of boats. Figure 3.3b demonstrates a standard reconstruction of the same image but from undersampled data. Aliasing artifacts in the image reconstruction are observed due to the sampling at a lower rate than Nyquist's, i.e., undersampling.

With the hope of removing such aliasing artifacts to obtain an exact reconstruction of the image, Candes, Romberg, and Tao conduct a puzzling numerical experiment [8]. In the experiment, they use the Shepp-Logan Phantom (Figure 3.4a), a simplified medical image of common use in medical analysis. Note that the measurements are taken in the frequency domain, i.e., Fourier coefficients are measured. After fully sampling the phantom, they randomly throw away 86% of the samples. Thus, they gathered 512 samples along each of the

(a) Original image     (b) Undersampled approximation

Figure 3.3: Boats: Original vs. traditional approximation of the undersampled image.

22 radial sampling lines (Figure 3.4b). To reconstruct the image from these samples, Candes et. al. apply a minimum energy $\ell_2$ reconstruction scheme defined by

$$\min_{\mathbf{x} \in \mathbb{C}^N} \quad \|\mathbf{x}\|_2$$
$$\text{subject to} \quad \Phi\mathbf{x} = \mathbf{y},$$

(3.2.1)

where $\Phi \in \mathbb{C}^{M \times N}$ is the measurement matrix, $\mathbf{x} \in \mathbb{C}^N$ is the vector of the reconstructed image, and $\mathbf{y} \in \mathbb{C}^M$ is the vector of the measured Fourier coefficients. The Fourier coefficients of the unobserved frequencies in this scheme are zeroed. As expected, applying a minimum energy reconstruction scheme to the undersampled data results in severe artifacts in the reconstructed image (Figure 3.4c). The obviously poor performance of that method diminishes its use for medical diagnostics. Candes et. al. suggest that the reconstruction will be with reduced artifacts if the Fourier transform coefficients of an image can be interpolated. However, the problem is that Fourier coefficients are difficult to predict from their neighbours due to the oscillatory nature of the Fourier transform. As an alternative, Candes et. al. propose a different reconstruction strategy based on minimizing the total variation (TV) (defined in Chapter 1

(1.2.4))

$$\min_{\mathbf{x}\in\mathbb{C}^N} \quad \|\mathbf{x}\|_{TV}$$
$$\text{subject to} \quad \Phi\mathbf{x} = \mathbf{y} \tag{3.2.2}$$

where $\Phi$ and $\mathbf{y}$ are defined as before. The idea of this strategy is to find a less complicated solution whose coefficients are a good match of the image coefficients while consistency with the observed data is maintained. The experiment gives surprisingly positive results as it justifies the hopes for an exact reconstruction (See Figure 3.4d) from far fewer than traditionally required samples. Hence, the motivation to develop what is today known as Compressive Sensing. More details on the minimization problems are presented in the next chapter.
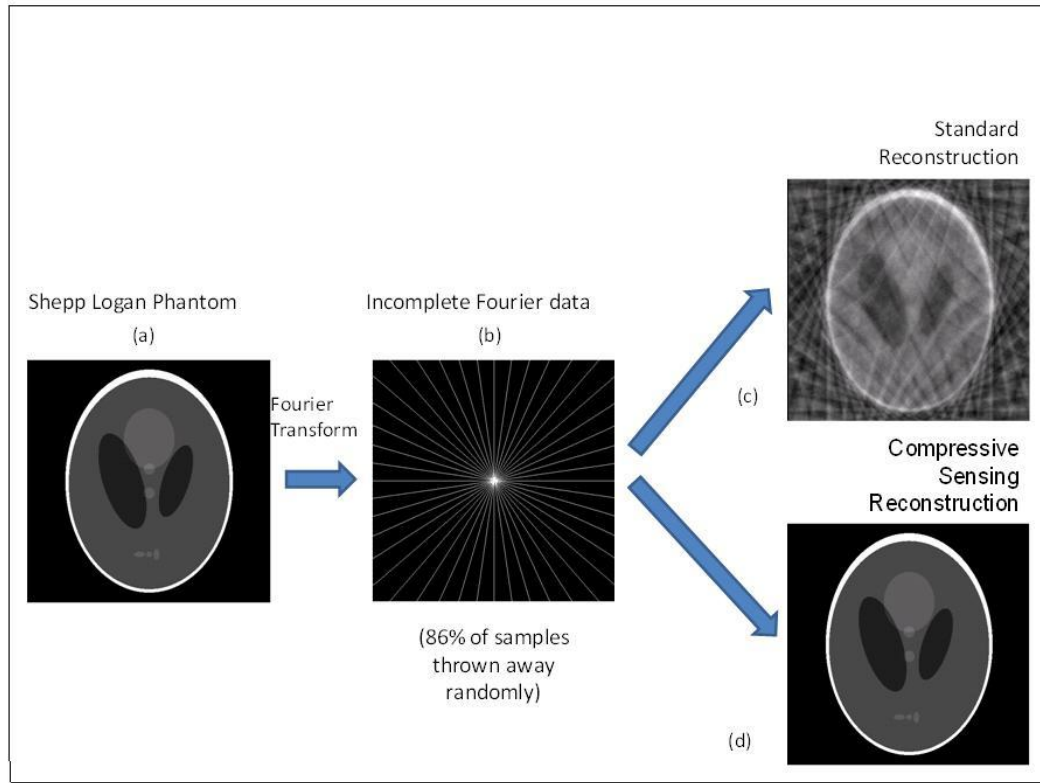


Figure 3.4: The experiment by Candes, Romberg, and Tao. (a) Shepp Logan phantom image. (b) Undersampled **k**-space along radial lines. (c) Minimum energy $\ell_2$ reconstruction. (d) Total Variation (TV) reconstruction.

## 3.3 Central Concept of CS

### 3.3.1 Introduction to the CS Problem

For simplicity, suppose the signal of interest is a one-dimensional vector $\mathbf{x} \in \mathbb{R}^{N \times 1}$ which we can think of as a discrete representation of a continuous signal sampled at over $N$ intervals. The domain of the signal may be time or space; in the one-dimensional case, we shall consider the domain to be temporal. Given an orthonormal basis $\{\boldsymbol{\psi_k}\}_{k=1}^{N}$, any vector $\mathbf{x} \in \mathbb{R}^{N \times 1}$ can be expanded in this basis according to the relation

$$\mathbf{x} = \sum_{k=1}^{N} s_k \boldsymbol{\psi_k} \quad \text{or} \quad \mathbf{x} = \Psi \mathbf{s}, \tag{3.3.1}$$

where $\Psi \in \mathbb{R}^{N \times N}$ is an orthogonal matrix with columns $\boldsymbol{\psi_1}$, $\boldsymbol{\psi_2}$, ..., $\boldsymbol{\psi_N}$ and $\mathbf{s}$ is the vector of coefficients of $\mathbf{x}$ in the basis $\{\boldsymbol{\psi_k}\}_{k=1}^{N}$. From (3.3.1) expressed as

$$\Psi^T \mathbf{x} = \mathbf{s}, \tag{3.3.2}$$

each element $s_i$ can be written as

$$s_i = \langle \mathbf{x}, \boldsymbol{\psi_i} \rangle. \tag{3.3.3}$$

Many natural signals, when expanded in a proper basis (e.g. short-time Fourier transform (STFT), Gabor transform, Wigner Distribution Function (WDF), S-Transform), contain relatively few large transform coefficients $s_i$. Those coefficients, $K$ in number, $(K \ll N)$ are the ones which capture most of the signal energy. Logically, one would expect that eliminating the remaining $(N - K)$ smallest $s_i$ coefficients would not cause perceptual loss in the signal. Signals with $K$ large and $(N - K)$ zero or approximately zero coefficients are $K - sparse$ or *compressible* signals, respectively. In mathematical language, if the sorted magnitudes $s_i$ of a given vector $\mathbf{s} \in \mathbb{R}^{N \times 1}$ decay quickly and $P_K \mathbf{s} \in \mathbb{R}^{N \times 1}$ is the $K$-sparse vector whose nonzero entries are the largest entries of $\mathbf{s}$, (i.e., all the $(N - K)$ smallest entries have been replaced by

zeros), then, the vector $P_K\mathbf{s}$, will approximate $\mathbf{s}$ well. Then, using $P_K\mathbf{s}$ and a matrix $\Psi$ as defined above, vector $\mathbf{x}$ can be approximated as $P_K\mathbf{x} \in \mathbb{R}^{N\times 1}$

$$P_K\mathbf{x} := \Psi P_K\mathbf{s}. \tag{3.3.4}$$

Since $\Psi$ is an orthonormal matrix,

$$\| \mathbf{x} - P_K\mathbf{x} \|_2 = \| \mathbf{s} - P_K\mathbf{s} \|_2 . \tag{3.3.5}$$

Then, if $\mathbf{x}$ is sparse, i.e., (3.3.4) is fulfilled , the error of approximation

$$\text{error} = \| \mathbf{x} - P_K\mathbf{x} \|_2 \tag{3.3.6}$$

will be small. To summarize, sparsity/compressibility of objects is a key property in the process of CS for two main reasons. First, the perceptual loss in the image approximation remains unnoticeable. The approximation is obtained by thresholding or throwing away a large fraction of the transform coefficients, i.e., the coefficients of our object of interest in a domain in which it has a sparse representation or is compressible. Here is an example. Figure 3.5(a) displays a one megapixel image. Its wavelet coefficients are plotted on Figure 3.5(b). The relatively few largest wavelet coefficients classify the image as compressible in the wavelet domain. Figure 3.5(c) shows an image approximation reconstructed from the largest 25,000 wavelet coefficients by zeroing the remaining ones. The difference between the original image and the approximation is unnoticeable. Back to the importance of sparsity/compressibility, knowing that most of the energy of a signal is in a few coefficients, one can aim to acquire specifically those coefficients, thus, reducing the measurements.

## 3.3.2   Sampling Mechanism

To give an idea of the sampling mechanism in CS setting, we introduce the sensing problem. What imaging devices most often capture in practice is not
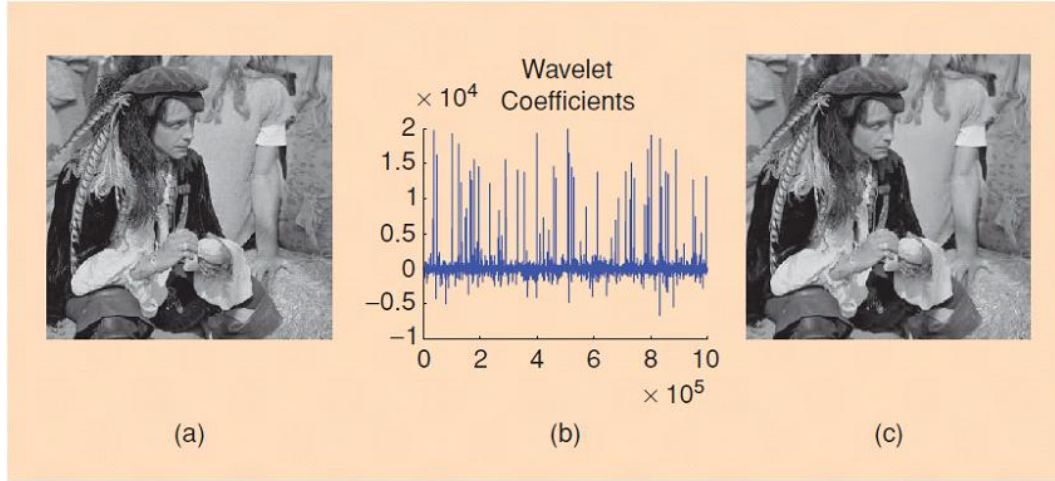
Figure 3.5: Example of compressible one megapixel image (a), its wavelet coefficients (b), and a perfect reconstruction of the image from the largest 25,000 wavelet coefficients (c).[7]

the original object $\mathbf{x}$, but a coded version of it, $\mathbf{y}$. Hence, their name *coded imaging systems*, as suggested by Romberg in [6]. Assuming vectors $\{\boldsymbol{\phi_k}\}_{k=1}^{M}$ are orthonormal, each measurement $y_k$ is an inner product of the original signal $\mathbf{x}$ and a test function $\boldsymbol{\phi_k}$:

$$y_1 = \langle \mathbf{x}, \boldsymbol{\phi_1} \rangle, \quad y_2 = \langle \mathbf{x}, \boldsymbol{\phi_2} \rangle, \quad ..., \quad y_M = \langle \mathbf{x}, \boldsymbol{\phi_M} \rangle. \tag{3.3.7}$$

Provided enough samples $M$ are acquired, the reconstruction of the object is successful. Three major inefficiencies inherent of the traditional sampling are described in CS literature [5, 6, 7, 8, 12]:

1. Even though the signal is compressible in that $K \ll N$ entries of $\mathbf{x}$ hold most of the energy, it is still necessary to take $M = N$ measurements $y_k$ $(k = 1, 2, \ldots, N)$.

2. If the signal $\mathbf{x}$ has sparse representation $\mathbf{s} = \Psi^T \mathbf{x}$, given $\mathbf{x}$, all $N$ coefficients $s_k$ of $\mathbf{s}$ need to be computed to find out which of the $K$ coefficients of $\mathbf{s}$ are nonzero (or large).

3. There is additional overhead required to encode the locations of the $K$ largest nonzero entries of $\mathbf{s}$.

As mentioned earlier in the chapter, CS deals with those disadvantages by directly acquiring the compressed signal representation with $M$ opposed to $N$ samples, where $M \approx K$ and $M \ll N$. One characteristic of the measurement process is the *measurement matrix* $\Phi \in \mathbb{R}^{M \times N}$, whose rows are formed by $\{\boldsymbol{\phi}_{\boldsymbol{k}}^{\boldsymbol{T}}\}_{k=1}^{M}$ so that

$$\mathbf{y} = \Phi\mathbf{x}. \qquad (3.3.8)$$

Substituting (3.3.1) in (3.3.8) reveals the relation between the measurements $\mathbf{y}$ and the original signal $\mathbf{x}$ through its sparse representation $\mathbf{s}$ (Figure 3.6)

$$\mathbf{y} = \Phi\Psi\mathbf{s} \qquad \text{or} \qquad \mathbf{y} = \Theta\mathbf{s}, \qquad (3.3.9)$$

where $\Theta = \Phi\Psi$, $\Theta \in \mathbb{R}^{M \times N}$. Equation (3.3.9) defines the essential problem in compressive sensing: given a vector of measurements $\mathbf{y} \in \mathbb{R}^{M \times 1}$ and a matrix $\Theta \in \mathbb{R}^{M \times N}$, determine a $K$-sparse vector $\mathbf{s} \in \mathbb{R}^{N \times 1}$ such that $\mathbf{y} = \Theta\mathbf{s}$ (where $K \leq M \ll N$). Various coded imaging systems use various types of test functions $\boldsymbol{\phi}_{\boldsymbol{k}}$: big pixels are measured in digital cameras, sinusoids are measured in MRI, line integrals are measured in CT, etc. In any case, choosing $\boldsymbol{\phi}_{\boldsymbol{k}}$ defines in which domain we collect information about the image of interest. $\boldsymbol{\phi}_{\boldsymbol{k}}$ is fixed for a particular image.

In our discussion so far, we have stated the CS problem. To solve it, one should consider two essential questions:

1. How can the measurement matrix be chosen to ensure that the reconstructed $K$-sparse vector $\mathbf{s}$ exists and is unique?

2. How can the resulting underdetermined linear system of equations be solved?
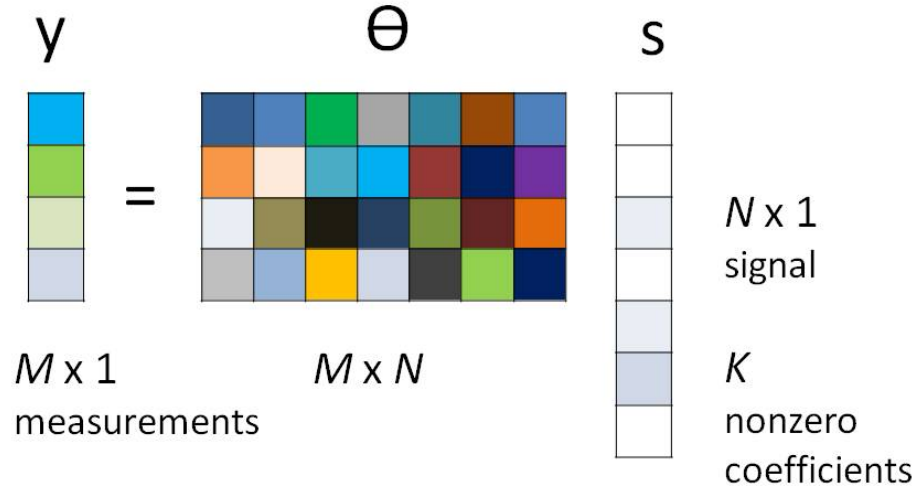
Figure 3.6: Signal encoding - Geometry of the measurement process: illustrates the relation of measurement vector $\mathbf{y}$, sparse representation of the signal $\mathbf{s}$, and matrix $\Theta = \Phi\Psi$.

### 3.3.3   Choosing the Measurement Matrix

The CS problem requires solving an underdetermined linear system of $M$ equations in $N$ unknowns. The solution $\mathbf{s}$ can be considered as the solution of an optimization problem, namely

$$\min_{\mathbf{s}\in\mathbb{R}^N} \quad \|\mathbf{s}\|_0$$
$$\text{subject to } \Theta\mathbf{s} = \mathbf{y} \tag{$P_0$}$$

where $\mathbf{y} \in \mathbb{R}^M$, and $\Theta$ is as previously defined. Since the solution of $(P_0)$ is generally nonunique, the problem is ill-posed. Finding a solution of $(P_0)$ seems hopeless at first. However, it is possible provided $\mathbf{s}$ is $K$-sparse and the locations of the $K$ nonzero coefficients are known. In addition, the so called *Restricted Isometry Property* (RIP) of order $K$ should hold.

**Definition 7.** [The Restricted Isometry Property]. Let $\Theta \in \mathbb{R}^{M \times N}$ be a matrix where $M < N$. Given $K < M$ and $\delta_K \in (0, 1)$, the matrix $\Theta$ is said to satisfy the Restricted Isometry Property of order $K$ with isometry constant $\delta_K$ if $\delta_K$ is the smallest positive number such that

$$(1 - \delta_K)\|\mathbf{s}\|_2^2 \leq \|\Theta\mathbf{s}\|_2^2 \leq (1 + \delta_K)\|\mathbf{s}\|_2^2 \qquad (3.3.10)$$

for all $K$-sparse vectors $\mathbf{s} \in \mathbb{R}^{N \times 1}$.

One way to interpret (3.3.10) is to say that the matrix $\Theta$ approximately preserves the length of $K$-sparse vectors, i.e., that $\Theta$ is approximately an isometry for $K$-sparse vectors. Equivalently, any subset of $K$ columns of $\Theta$ are almost orthogonal. In reality, a sufficient condition for a stable measurement matrix is the RIP of order $3K$. That is, the solution is exact if $\Theta$ satisfies (3.3.10) for an arbitrary vector $\mathbf{s}$ which is $3K$-sparse [4, 7]. An alternative criterion to the RIP for an effective sparse reconstruction is the *Uniform Uncertainty Principle* (UUP) [6].

**Definition 8.** [The Uniform Uncertainty Principle]. Let $\Theta \in \mathbb{R}^{M \times N}$ be a matrix where $M < N$. Given $K < M$, the matrix $\Theta$ is said to satisfy the Uniform Uncertainty Principle if for any $K$-sparse vector $\mathbf{h}$,

$$\frac{1}{2} \cdot \frac{M}{N} \cdot \|\mathbf{h}\|_2^2 \leq \|\Theta\mathbf{h}\|_2^2 \leq \frac{3}{2} \cdot \frac{M}{N} \cdot \|\mathbf{h}\|_2^2. \qquad (3.3.11)$$

That is, the energy of the measurements $\Theta\mathbf{h}$ will be comparable to the energy of $\mathbf{h}$ itself, where $\mathbf{h} = \mathbf{s} - \mathbf{s}'$ represents the difference between the $K$-sparse vector $\mathbf{s}$ and any other $K$-sparse (or sparser) vector $\mathbf{s}'$. Please note that to guarantee the uniqueness of the solution $\mathbf{s}$, $\mathbf{h}$ should be close to $\mathbf{0}$. Another condition applied in the design of $\Theta$, for an efficient CS, is the existence of incoherence between $\Phi$ and $\Psi$. As in [7], the *coherence* between the two basis is $\mu(\Phi, \Psi)$, defined by

$$\mu(\Phi, \Psi) = \sqrt{N} \cdot \max |\langle \boldsymbol{\phi_i}, \boldsymbol{\psi_j} \rangle|. \qquad (3.3.12)$$

In plain words, (3.3.12) reveals the largest correlation between any two columns of the matrices $\Phi$ and $\Psi$ used respectively to sense the object and to represent the object sparsely. Compressive sensing is interested in low largest correlation, which is the rows $\{\phi_i^T\}$ of $\Phi$ cannot sparsely represent the columns $\{\psi_j\}$ of $\Psi$ and vice versa. Interpreted in a different way, the low coherence requirement of CS is in fact a requirement for high incoherence. Linear algebra gives us the bounds for $\mu$, namely $\mu(\Phi, \Psi) \in [1, \sqrt{N}]$. Therefore, ideally, highest incoherence is achieved when $\mu(\Phi, \Psi) = 1$. The necessity of high incoherence is clarified in Theorems 1 and 2 in the next section.

Interestingly, random matrices $\Phi$ exhibit large incoherence with any fixed basis $\Psi$. Many matrices in fact satisfy the RIP, e.g. random waveforms with independent identically distributed (i.i.d.) entries (e.g. Gaussian, +- binary, etc.)[7]. In practice, a general rule in meeting the high incoherence requirement can be considered making $\Phi$ unstructured w.r.t. $\Psi$. It turns out if measurement matrix $\Phi$ is chosen at random, the aforementioned RIP and incoherence conditions are achieved with high probability [5].

### 3.3.4 Signal Reconstruction Framework

Effective data acquisition is useless without a working mechanism for an accurate reconstruction of the object. If the RIP holds, then the problem of solving $(P_0)$ is almost always equivalent to solving the convex program known as *basis pursuit (BP)*[20], namely

$$\min_{\mathbf{s} \in \mathbb{R}^N} \|\mathbf{s}\|_1 \qquad \text{subject to} \qquad \Theta\mathbf{s} = \mathbf{y}. \qquad \text{(BP)}$$

In words, the $M$ measurements in the data vector $\mathbf{y}$ are recovered in such a way that the reconstructed signal $\mathbf{s}$ has the sparsest representation. While minimization of $\mathbf{s}$ in the $\ell_1$-norm enforces sparsity, the linear constraint ensures data consistency. In the last decade, a series of papers by Donoho et al., Nemirovski, Gribonval [27, 28, 29] have introduced the minimization of $\ell_1$-norm

and explain why it could recover sparse signals in a special setup. A notion of why $\ell_1$-minimization is an efficient substitute for the sparsity is illustrated through the geometry of the $\ell_1$-minimization problem on Figure 3.8 [6]. Due to the anisotropy of $\ell_1$ unit ball, one lands on a sparse solution of the minimization problem (2D case in this example).

Candes and Wakin [7] suggest an efficient data acquisition protocol regulated by two theorems.

**Theorem 1.** *[Candes, Romberg, Tao, 2004]. Let* $\mathbf{x} = \Psi\mathbf{s}$, $\mathbf{x} \in \mathbb{R}^N$ *be* $K$-sparse *in domain* $\Psi$. *Let* $\Omega \subset \{1, \dots, N\}$ *be a set of* $M$ *Fourier coefficient indices. Consider the* $\ell_1$ *minimization problem*

$$\min_{\widetilde{\mathbf{s}} \in \mathbb{R}^N} \|\mathbf{s}\|_1 \qquad subject\ to \qquad y_k = \langle \boldsymbol{\phi_k}, \Psi\mathbf{s} \rangle, \quad \forall k \in \Omega.$$

*Select* $M$ *measurements in the* $\Phi$ *domain uniformly at random. Then, if*

$$M \geq C \cdot \mu^2(\Phi, \Psi) \cdot K \cdot \log N \tag{3.3.13}$$

*for some positive constant* $C$, *the problem has a unique solution* $\mathbf{s}^*$ *with overwhelming probability and* $\mathbf{s}^* = \mathbf{s}$.

In plain language, Theorem 1 states that a signal with a $K$-sparse representation in the transform domain can be recovered exactly with overwhelming probability from randomly chosen $M$ samples and for some positive constant $C$, provided (3.3.13) holds.

**Theorem 2.** *[Candes, 2008]. If* $\Theta \in \mathbb{R}^{M \times N}$ *satisfies the RIP of order* $2K$ *with the isometry constant* $\delta_{2K} < \sqrt{2} - 1$, *then, for all vectors such that* $\Theta\mathbf{s} = \mathbf{y}$, *the solution* $\mathbf{s}^*$ *of* (BP) *satisfies*

$$\|\mathbf{s}^* - \mathbf{s}\|_2 \leq \frac{C_0}{\sqrt{K}} \|\mathbf{s} - P_K\mathbf{s}\|_1$$

$$and \tag{3.3.14}$$

$$\|\mathbf{s}^* - \mathbf{s}\|_1 \leq C_0 \cdot \|\mathbf{s} - P_K\mathbf{s}\|_1$$

*where* $P_K\mathbf{s}$ *is the best* $K$-sparse *approximation of* $\mathbf{s}$. *In particular, if* $\mathbf{s}$ *is* $K$-sparse, *the solution of* $(P_0)$ *is exact.*

Theorem 2 asserts that, regardless of signal's sparsity, the quality of its reconstruction is not worse compared to the case in which the locations and values of the $K$-largest coefficients of $\mathbf{s}$ were known. Moreover, no probability is involved, i.e., the $K$-largest elements of all vectors is guaranteed to be recovered with no probability of failure. In the sense that Theorem 2 deals with the reconstruction of all signals, it is a more general and stronger result.

Equation (3.3.13) of Theorem 1 justifies the requirement of high incoherence. When $\mu = 1$, the fewest number of samples $M = K \log N$ needed for exact reconstruction , with practically zero probability of failure, is achieved. A practical rule from the empirical successful reconstructions is extracted: $M \sim 5$ $- 6K$. We demonstrate the requirement for the lowest number of measurements in an example (Figure 3.7). A sparse signal, $K = 63$, of length $N = 1683$ (Figure 3.7a) undergoes $\ell_2$ and $\ell_1$ recovery, respectively. Figures 3.7b and 3.7c demonstrate the reconstruction from random 252 samples ($M = 4K$). Figures 3.7d and 3.7e demonstrate the reconstruction from random 467 samples ($M = K \log N \sim 7.5K$). Figures 3.7f and 3.7g demonstrate the reconstruction from random 630 samples ($M = 10K$). The figures in the right column show that while the reconstruction from fewer than $5K$ samples has a degraded quality, the reconstructions from number of samples for which the practical rule is applied are almost exact.

In summary, solving the optimization problem (BP) achieves two goals:

1. Identifies which coefficients of $\mathbf{s}$ are significant (i.e. the sparsity structure of $P_K \mathbf{s}$).

2. Recovers the vector $\mathbf{s}$.
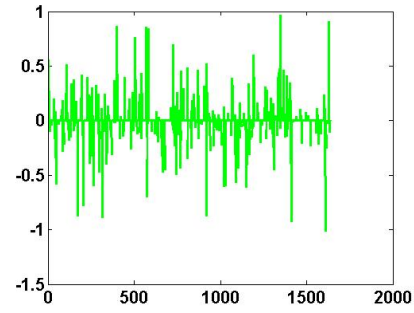
It is worth mentioning that $\ell_1$-norm minimization is not the only way of recovering an image from sparse samples. Some other well-established techniques for CS are matching pursuit, iterative thresholding, total-variation minimization,
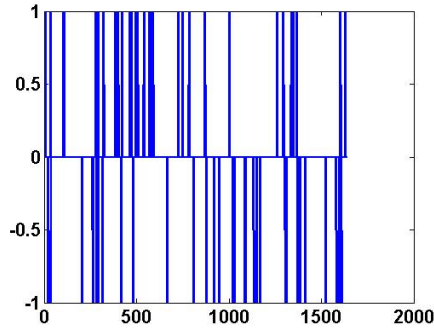
(a) original signal
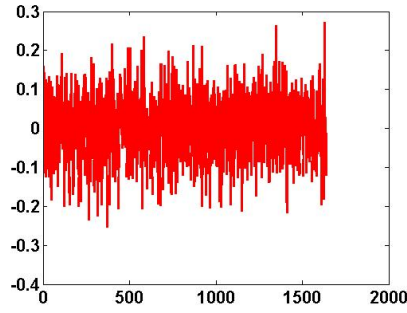


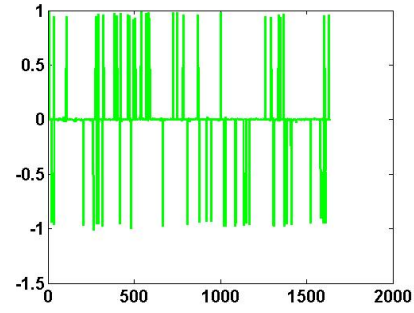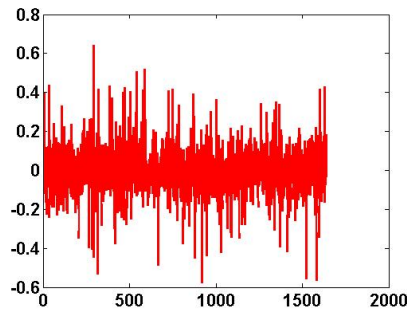(b) $\ell_2$ reconstruction from $M = 252$    (c) $\ell_1$ reconstruction from $M = 252$
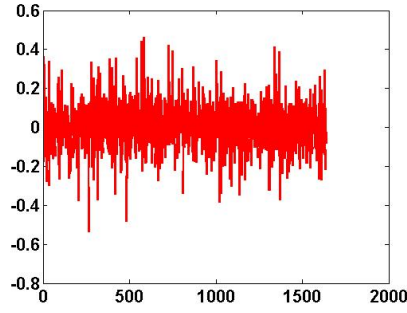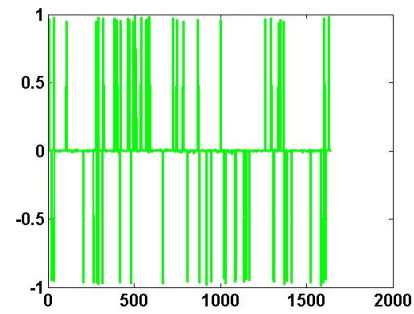


(d) $\ell_2$ reconstruction from $M = 467$    (e) $\ell_1$ reconstruction from $M = 467$



(f) $\ell_2$ reconstruction from $M = 630$    (g) $\ell_1$ reconstruction from $M = 630$

Figure 3.7: Practical rule: Finding fewest number of samples $M$ for a $K$-sparse signal of length $N$ /$K = 63$, $N = 1683$/.

and greedy algorithms [24, 25, 20, 26]. They all have advantages and disadvantages in the variety of applications. For example, matching pursuit is very fast for small-scale problems, but not as accurate for large-scale ones in the presence of noise. Iterative thresholding, a method similar to the $\ell_1$ minimization method, is very fast. It recovers sparse signals very well and approximately sparse signals moderately well. While total-variation minimization is accurate and robust for recovering images, it can be slow [13].
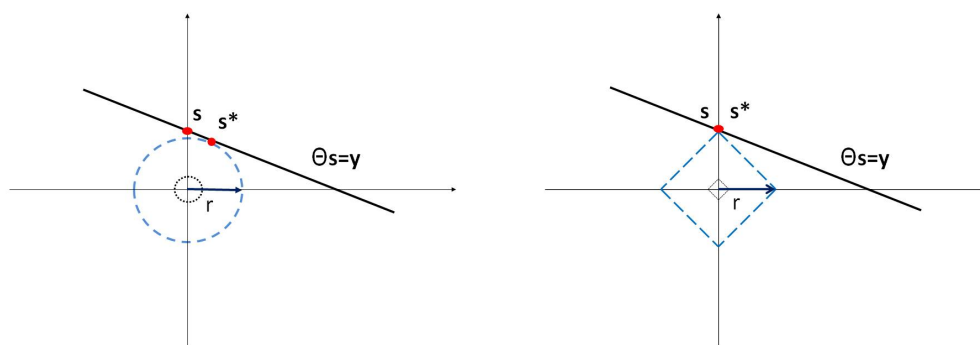


(a) $\ell_2$ solution of (BP)- the point of contact $\mathbf{s}^*$ between $\ell_2$ unit ball and null space $H$

(b) $\ell_1$ solution of (BP)- the point of contact $\mathbf{s}^*$ between $\ell_1$ unit ball and null space $H$

Figure 3.8: Visualization of $\ell_2$ vs. $\ell_1$ solution of (BP).

## 3.4 An Intuitive Example

The apparent ability to reconstruct signals from undersampled data using the framework of compressed sensing is not without conditions. Compressed sensing permits undersampled signal recovery when certain key ingredients are present:

1. Sparsity, i.e., the signal to be reconstructed is sparse in some suitable domain;

2. Incoherence, i.e., the basis vectors in the domain in which the signal is sparse are incoherent with the columns of the measurement matrix; and

3. Suitable optimization algorithms exist to solve related reconstruction problems.

Sparsity can be implicit. The signal itself may need to be mapped to some other domain in which its representation is sparse, i.e., $\mathbf{x} = \Psi \mathbf{s}$ where $\mathbf{s}$ is K-sparse with $\Psi$ not equal to $I$. On the other hand, if $\mathbf{x}$ is already sparse, then $\Psi = I$ and $\mathbf{x}$ is explicitly sparse. Most MRI images are implicitly sparse. Examples of medical images that are explicitly sparse include images of blood vessels and angiograms.

To demonstrate how those ingredients blend and to show the importance of compressibility as well as incoherence, we consider an example (Figure 3.9).

- We consider a 1D signal of length $N = 256$ which is $K$-sparse in the image domain with $K = 3(1)$.

- The **k**-space of the signal is undersampled, i.e., a $K$-sparse vector is extracted from the DFT of the original vector. The undersampling is done in two different ways: a) uniformly (traditional in signal processing) and b) pseudo-randomly (2).

- The zero-filled Fourier reconstruction of the uniformly undersampled **k**-space of the image results in uniform aliasing pattern. Due to the ambiguity the recovery of the original signal is hopeless (3a).

- The zero-filled Fourier reconstruction of the pseudo-randomly undersampled **k**-space of the image displays incoherent (noise-like) artifacts while preserving most of the largest components. Those artifacts are the leakage of energy away from each individual nonzero value of the original signal to the other reconstructed signal coefficients, including to the true zeros in the original signal. Based on the knowledge of the **k**-space sampling scheme and the original signal, the leakage can be calculated analytically (3).

- After setting an appropriate level of interference (threshold), the components standing out above the level of interference are detected (4) and recovered (5).

- The interference of the recovered components is computed assuming the original signal consisted only of those few detected values (6).

- The interference of the recovered largest coefficients is eliminated by subtracting it from the interference obtained before recovering them.That adjusts the interference to a lower level and enables recovery of smaller coefficients (7). The process is iterative and is repeated until all significant components are recovered.
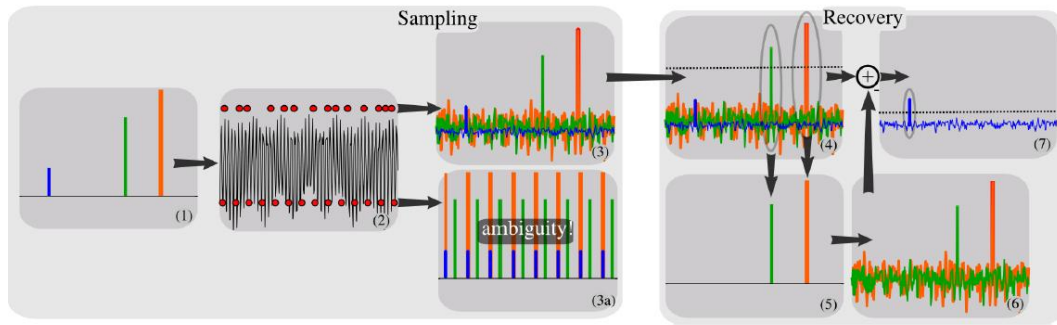


Figure 3.9: Heuristic recovery procedure for an undersampled signal.[4]

## 3.5 MRI as a Compressive Sensing System

While improvement in MRI data acquisition speed is important, it is limited due to physical and physiological constraints. There are certain questions that need to be addressed in order to figure out whether or not MRI can benefit from compressive sensing.

- Are MR images sparse (somehow)?

- Do the measurements made somehow correspond to a measurement matrix that satisfies the RIP?

- Is it possible to solve the corresponding minimization problem somehow?

The first two requirements are necessary to invoke the key theorems, i.e., that the underdetermined sparse recovery problem can be achieved by solving an appropriate convex program. That is, the first two requirements are about whether or not we can reformulate the problem. The last requirement is about algorithms to solve the problem once it is reformulated. This last consideration is not really strongly limited by the technological limitations of MRI per se.

Recently, the necessity of compressing images for various reasons developed successful image compression tools such as JPEG, JPEG-2000, and MPEG. The appropriately chosen sparsifying transforms have an essential role in those tools as they map the image vector into a sparse vector. Discrete Cosine Transform (DCT) (basis for JPEG), wavelets (basis for JPEG-2000), and finite-differences (basis for MPEG) are amongst the most effective sparsifying transforms underlying the above-mentioned compression standards [11]. The results of the ongoing research build a library; it stores information on possible and effective sparsifying transformations for many and different types of images [2] [10]. The records in this library show that natural and medical images are susceptible to compression in a known transform domain with no or minor loss of information [9]; common transform domains in which most MR images reveal sparsity are DCT, wavelets, etc.

Moreover, one can get adaptive approximation performance from a fixed set of measurements by changing the sparsifying domain, depending on the goals pursued by the approximation. Therefore, one can assume the first CS ingredient for a sparse representation of the desired object in a known transform domain is fulfilled. Lustig et al. (2007) provide examples of transform sparsity

of MR images. By compressing the fully sampled images of a brain, angiogram, and dynamic heart, using the largest wavelet, finite-differences, and temporal-frequency coefficients, they reconstruct an approximation of those images from the corresponding transform coefficients. The experiment illustrates that the amount of the largest coefficients, carrying the most of the energy in those images, constitute respectively 10%, 5% and 5% of all captured coefficients (See Figure 3.10).
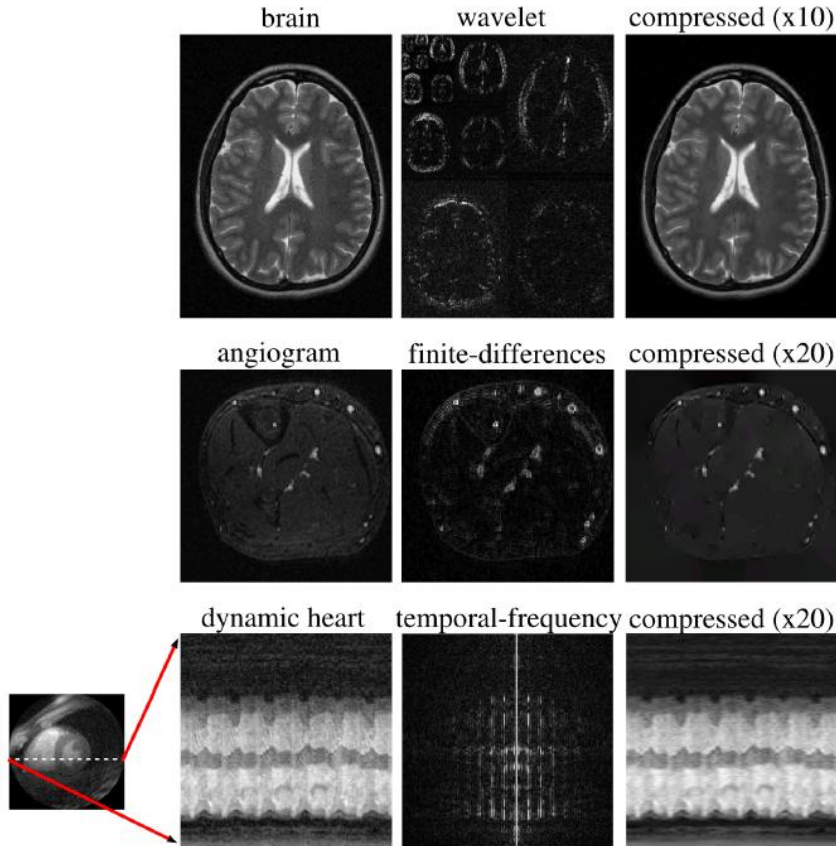


Figure 3.10: Illustration of MR images transform sparsity: Fully sampled images (left column); same images in the corresponding transform domain (middle column); the reconstructed images from 10%, 5%, and 5% of all captured coefficients .[2]

Recall each measurement $y_k$ is a linear combination of the original image $\mathbf{x}$ and a test function $\boldsymbol{\phi_k}$ (3.3.7). MRI scanners acquire the samples in the spatial frequency domain (i.e., the Fourier or $\mathbf{k}$-space domain) rather than the pixel domain. Thereafter, MRI scanners can be viewed as natural coded imaging

systems that measure Fourier coefficients (**k**-samples). This qualifies MRI systems as a special case of CS, sampling a subset of the image **k**-space.

It remains to demonstrate the incoherence between the transform domain (the domain in which the object has a sparse representation) and the frequency domain (the domain in which the measurements are actually taken). In their original paper [8], the authors of CS theory suggest that random undersampling of **k**-space guarantees high incoherence of the signal in the transform domain. It is worth noting that **k**-trajectories need to be relatively smooth. To ensure this requirement, in practice, not all dimensions are undersampled. With this limitation in mind, MRI scientists develop working trajectories in a way that random undersampling, generating incoherent interference, is mimicked. Some common trajectories have been introduced in Chapter 2 of this thesis and comments have been made on applications appropriateness for each trajectory.

Designing optimal trajectories is beyond the scope of this thesis. For the purposes of the experiments here, we use Monte-Carlo Incoherent Sampling Design suggested in [2]. In brief, it takes into account the fact that most of the energy of the natural images (MR images included) is concentrated around the **k**-space origin. Thus, undersampling less near the **k**-space origin and more in the periphery provides better incoherence performance of the sampling scheme. Lustig's Monte-Carlo Incoherent Sampling Design allows for choosing the samples randomly with sampling density diminishing with a power of distance from the origin.

Figure 3.11 summarizes the CS image reconstruction procedure in an MRI system. The original image undergoes Fourier undersampling. Then, it is transformed back to the original domain. If the image is sparse there, a non-linear reconstruction is applied to obtain the recovered image. In case the image is not sparse, it is mapped into a sparsifying domain. Then, it is recovered by a non-linear reconstruction scheme.
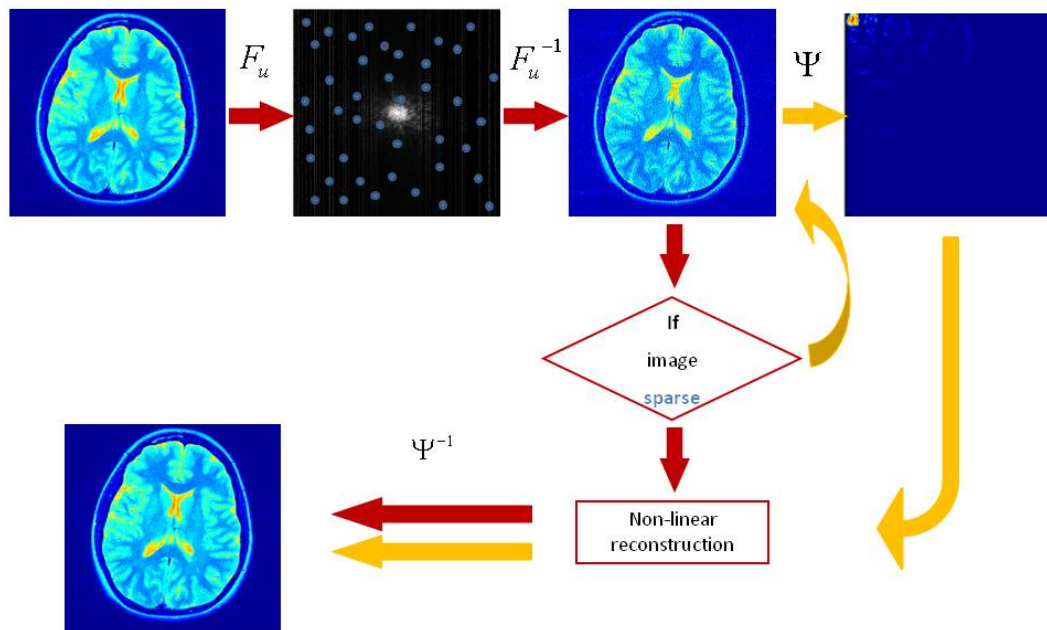
Figure 3.11: CS procedure in an MRI system.

# Chapter 4

# Optimization Algorithms for Sparse MRI Reconstruction

## 4.1 Convex Optimization Terminology

What makes compressive sensing a feasible framework for image reconstruction is the fact that the problem of sparse image reconstruction can be reformulated as the constrained optimization problem (BP). This is in fact an example of a convex optimization problem. For clarity, we review some ideas from the optimization literature before discussing algorithms.

A *constrained optimization problem* is a problem of the form

$$\min_{\mathbf{x} \in \mathbb{R}^n} \quad f_0(\mathbf{x})$$
$$\text{subject to} \quad f_i(\mathbf{x}) \le b_i, \qquad i = 1, \dots, m. \tag{4.1.1}$$

where $\mathbf{x} \in \mathbb{R}^n$ is the vector of the *optimization variables*, the function $f_0 : \mathbb{R}^n \to \mathbb{R}$ is the *objective function*, the functions $f_i : \mathbb{R}^n \to \mathbb{R}$ are the *constraint functions*, and the constants $b_1, \dots, b_m \in \mathbb{R}$ are the limits, or bounds, for the constraints [13]. It is also possible to have equality constraints.

A vector $\mathbf{x}^*$ is said to be an *optimal solution* of the optimization problem when $f_0(\mathbf{x}^*)$ has the smallest value among all vectors that satisfy the constraints.

In the absence of constraints, the problem is defined as an *unconstrained optimization problem.*

A function $f(\mathbf{x})$ is a *convex function* if it satisfies

$$f(\alpha\mathbf{x} + \beta\mathbf{y}) \le \alpha f(\mathbf{x}) + \beta f(\mathbf{y}) \tag{4.1.2}$$

for all $\mathbf{x}$, $\mathbf{y} \in \mathbb{R}^n$ and all $\alpha$, $\beta \in \mathbb{R}$ with $\alpha + \beta = 1$, $\alpha \ge 0$, $\beta \ge 0$.

A *convex optimization problem* is a constrained optimization problem in which the objective function $f_0$ and the constraint functions $f_1, \ldots, f_m$ are all convex functions.

In the event that the equality holds in (4.1.2), i.e.,

$$f_i(\alpha\mathbf{x} + \beta\mathbf{y}) = \alpha f_i(\mathbf{x}) + \beta f_i(\mathbf{y}) \tag{4.1.3}$$

for all $\mathbf{x}$, $\mathbf{y} \in \mathbb{R}^n$ and all $\alpha$, $\beta \in \mathbb{R}$, the problem is called a *linear program* which is a special case of a convex problem. If the constrained optimization problem is not linear, it is a *nonlinear program.*

*Linear programming* is a class of optimization problems in which the objective and all constraint functions are linear. It has the form

$$\begin{aligned} \min_{\mathbf{x}\in\mathbb{R}^n} \quad & \mathbf{c}^T\mathbf{x} \\ \text{subject to} \quad & \mathbf{a_i}^T\mathbf{x} \le b_i, \qquad i = 1, \ldots, m. \end{aligned} \tag{4.1.4}$$

Here the vectors $\mathbf{c}, \mathbf{a}_1, \ldots, \mathbf{a}_m \in \mathbb{R}^n$, and scalars $b_1, \ldots, b_m \in \mathbb{R}$ are problem parameters that specify the objective and constraint functions.

A *second-order cone program* (SOCP) [13] is an optimization problem of the form

$$\begin{aligned} \min_{\mathbf{x}\in\mathbb{R}^n} \quad & \mathbf{f}^T\mathbf{x} \\ \text{subject to} \quad & \|A_i\mathbf{x} + \mathbf{b}_i\|_2 \le \mathbf{c}_i^T\mathbf{x} + d_i, \qquad i = 1, \ldots, m \\ & F_j\mathbf{x} = \mathbf{g}_j, \qquad j = 1, \ldots, r \end{aligned} \tag{4.1.5}$$

where $\mathbf{x} \in \mathbb{R}^n$ is the optimization variable, $\mathbf{f} \in \mathbb{R}^n$, $A_i \in \mathbb{R}^{n_i \times n}$, $\mathbf{b}_i \in \mathbb{R}^{n_i}$, $\mathbf{c}_i \in \mathbb{R}^n$, $d_i \in \mathbb{R}$ are the parameters of the inequality constraints of the problem,

and $F_j \in \mathbb{R}^{p \times n}$, $\mathbf{g}_j \in \mathbb{R}^p$ are the parameters of the equality constraints of the problem.

A constraint of the form

$$\|A\mathbf{x} + \mathbf{b}\|_2 \leq \mathbf{c}^T\mathbf{x} + d, \tag{4.1.6}$$

with $A \in \mathbb{R}^{k \times n}$ is called a *second-order cone constraint* since it is the same as requiring the affine function $(A\mathbf{x} + \mathbf{b}, \mathbf{c}^T\mathbf{x} + d)$ to lie in the second-order cone in $\mathbb{R}^{k+1}$. For more explicit examples, refer to [14].

## 4.2 Convex Optimization for a Sparse Signal Reconstruction

As we mentioned at the beginning of the chapter, the problem of sparse signal reconstruction can be recast as a convex optimization problem. Ideally, the signal of interest exhibits strong sparsity and its sampling is noise-free. In practice, however, general objects of interest are approximately sparse and a certain level of noise in data acquisition affects the object approximation. To account for these two circumstances, the optimization problem (BP) introduced earlier is now reformulated as the convex problem

$$\begin{aligned} \min_{\mathbf{x} \in \mathbb{R}^n} \quad & \|\mathbf{x}\|_1 \\ \text{subject to} \quad & \|\mathbf{b} - A\mathbf{x}\|_2 \leq \varepsilon, \end{aligned} \tag{4.2.1}$$

where $\mathbf{x} \in \mathbb{R}^n$ is the sparse object of interest to be reconstructed, $A \in \mathbb{R}^{m \times n}$ is the known measurement matrix, $\mathbf{b} \in \mathbb{R}^m$ is the measured data, and $\varepsilon$ is the noise threshold parameter which is easy to estimate in real situations. While the anisotropy of the $\ell_1$ norm ensures sparsity of the reconstructed image $\mathbf{x}$, the isotropy of the $\ell_2$ norm, used in the (4.2.1) constraint, ensures the data is consistent with the measurements while the recovered image is kept at the required accuracy (the error of approximation is below $\varepsilon$). The equivalent dual

problem of problem (4.2.1) is

$$\max_{\mathbf{z}\in\mathbb{R}^m} \quad \mathbf{b^T z} + \varepsilon w$$
$$\text{subject to} \quad A^T\mathbf{z} = f \tag{4.2.2}$$
$$\|\mathbf{z}\|_2 \leq w$$

Provided (4.2.1) is recast as an unconstrained problem through logarithmic barrier function with log-barrier parameter $\tau$, the point $(\mathbf{z}^*(\tau), w^*(\tau))$ is strictly feasible. The duality gap, $2/\tau$ in this case, is associated with the optimal points $\mathbf{x}^*$ and $(\mathbf{z}^*(\tau), w^*(\tau))$. (For more details on primal and dual problems refer to [13].)

The problem (4.2.1) can be recast as a second-order cone program (SOCP) and can be solved efficiently (as advocated in [7, 13, 14, 15]). Becker and Candes in [16] suggest two other equivalent forms to problem (4.2.1). The first reformulation of the sparse recovery problem, known as basis pursuit denoising problem (BPDN), is an unconstrained problem in the so called Lagrangian form

$$\min_{\mathbf{x}\in\mathbb{R}^n} \quad \lambda\|\mathbf{x}\|_1 + \frac{1}{2}\|\mathbf{b} - A\mathbf{x}\|_2^2 \tag{4.2.3}$$

where $\lambda$ is a regularization parameter that determines the trade-off between the data consistency and sparsity. $\lambda$ can be adjusted in such a way using $\tau$ that the solution of (4.2.3) is an exact solution of (4.2.1) as well.

A third approach of solving the sparse reconstruction, used mainly in statistics, is known as LASSO and is of the form:

$$\min_{\mathbf{x}\in\mathbb{R}^n} \quad \|\mathbf{b} - A\mathbf{x}\|_2$$
$$\text{subject to} \quad \|\mathbf{x}\|_1 \leq \tau. \tag{4.2.4}$$

Lustig [2] in his original work solves the problem of sparse MRI reconstruction by reformulating (4.2.3) as an unconstrained problem using a penalty method and using a nonlinear conjugate-gradient solver. To avoid this penalty reformulation, with the hopes of improving performance, we choose to experiment

with alternative solvers to the directly SOCP formulation (4.2.1). As Becker and Candes argue, being able to solve problem (4.2.1) is especially important from a practical point of view. Compared to solving the unconstrained problem (4.2.3), solving the quadratically constrained problem (4.2.1) is much more difficult [13]. However, estimating $\varepsilon$ is more feasible than estimating $\lambda$. In their technical report, Becker and Candes point to several publicly available online state-of-the-art optimization techniques for solving (4.2.1) or (4.2.3) (e.g., GPSR, SpaRSA, Bregman, FPC). Of all competitive algorithms, we choose to experiment with NESTA and $\ell_1$- MAGIC as the only methods dealing directly with the SOCP formulation.

## 4.3 SOCP-LB Solver with Log-barrier Method

The software package $\ell_1$- MAGIC [17] can be used to recover sparse signals by recasting certain problems as SOCPs using log-barrier method; however, it cannot handle complex data directly. Since the sparse MRI reconstruction problem we wish to solve is an optimization problem involving complex data and decision variables, we implement the log-barrier method in our own SOCP-LB solver adopting the techniques used in $\ell_1$- MAGIC . Specifically in our problem, given $\epsilon \geq 0$, $\mathbf{b} \in \mathbb{C}^{M \times 1}$, and $A \in \mathbb{C}^{M \times N}$, we wish to determine

$$\min_{\mathbf{x} \in \mathbb{C}^N} \quad \|\mathbf{x}\|_1$$

$$\text{subject to } \|A\mathbf{x} - \mathbf{b}\|_2 \leq \epsilon. \tag{$P_1$}$$

The data $\mathbf{b}$ and $A$ can be used to define corresponding real data $\mathbf{h} \in \mathbb{R}^{2M \times 1}$ and $G \in \mathbb{R}^{2M \times 3N}$ according to

$$\mathbf{h} \quad := \quad \begin{bmatrix} \text{Re}(\mathbf{b}) \\ \text{Im}(\mathbf{b}) \end{bmatrix} \text{ and} \tag{4.3.1a}$$

$$G \quad := \quad \begin{bmatrix} \text{Re}(A) & -\text{Im}(A) & \mathbf{0} \\ \text{Im}(A) & \text{Re}(A) & \mathbf{0} \end{bmatrix} \tag{4.3.1b}$$

where $\mathbf{0} \in \mathbb{R}^{M \times N}$. With the data $\mathbf{h}$ and $G$ as defined in (4.3.1) and the threshold $\epsilon > 0$, we define a related optimization problem involving real decision variables, namely

$$\min_{\mathbf{z} \in \mathbb{R}^{3N}} \mathbf{c}^T \mathbf{z} \text{ subject to}$$

$$\|G\mathbf{z} - \mathbf{h}\|_2 \le \epsilon, \qquad \qquad , \qquad \qquad (P_2)$$

$$\sqrt{[z_k]^2 + [z_{k+N}]^2} \le z_{k+2N} \qquad (k = 1, \dots, N)$$

where the vector $\mathbf{c} \in \mathbb{R}^{3N}$ in the objective function of $(P_2)$ is given in blocks by

$$\mathbf{c} := \begin{bmatrix} \mathbf{0} \\ \mathbf{0} \\ \mathbf{e} \end{bmatrix} \text{ with } \mathbf{0} \in \mathbb{R}^{N \times 1} \text{ and } \mathbf{e} := \begin{bmatrix} 1 \\ 1 \\ \vdots \\ 1 \end{bmatrix} \in \mathbb{R}^{N \times 1}. \qquad (4.3.2)$$

Observe that the complex data $\mathbf{b}$ and $A$ for $(P_1)$ uniquely determine the real data $\mathbf{h}$ and $G$ for $(P_2)$; the converse is also true provided that $G$ has the appropriate antisymmetric block structure.

We can now prove the following proposition.

**Proposition 1.** *Let* $\mathbf{x}^\star \in \mathbb{C}^N$ *be the minimizer of* $(P_1)$ *with corresponding minimum value* $m^\star = \|\mathbf{x}^\star\|_1$. *Let* $\mathbf{z}^{\star\star} \in \mathbb{R}^{3N}$ *be the minimizer of* $(P_2)$ *with corresponding minimum value* $m^{\star\star} = \mathbf{c}^T \mathbf{z}^{\star\star}$. *Then* $m^\star = m^{\star\star}$, *i.e., the minimum values attained in solving* $(P_1)$ *and* $(P_2)$ *are equivalent.*

*Proof.* Given the minimizer $\mathbf{x}^\star \in \mathbb{C}^N$ of $(P_1)$, define the vector $\mathbf{z}^\star \in \mathbb{R}^{3N \times 1}$ by

$$\mathbf{z}^\star := \begin{bmatrix} \mathbf{u}^\star \\ \mathbf{v}^\star \\ \mathbf{t}^\star \end{bmatrix}, \text{ with } u_k^\star := \text{Re}(x_k^\star), v_k^\star := \text{Im}(x_k^\star), \text{ and } t_k^\star := |x_k^\star| \quad (k = 1, \dots, N).$$

By construction of $\mathbf{z}^\star$,

$$\|G\mathbf{z}^\star - \mathbf{h}\|_2 = \|A\mathbf{x}^\star - \mathbf{b}\|_2 \le \epsilon,$$

as obtained by expanding out the complex matrix-vector product and applying the definitions in (4.3.1). Furthermore, the construction of $\mathbf{z}^\star$ implies that, for $k = 1, \ldots, N$,

$$\sqrt{[z_k^\star]^2 + [z_{k+N}^\star]^2} = \sqrt{[\text{Re}(x_k^\star)]^2 + [\text{Im}(x_k^\star)]^2}$$
$$= |x_k^\star|$$
$$= z_{k+2N}^\star;$$

that is,

$$\sqrt{[z_k^\star]^2 + [z_{k+N}^\star]^2} \leq z_{k+2N}^\star \quad (k = 1, \ldots, N).$$

Then $\mathbf{z}^\star$ is a feasible point for $(P_2)$. Since the minimum value $m^{\star\star}$ of the objective function in $(P_2)$ is attained at $\mathbf{z}^{\star\star}$, we have

$$m^{\star\star} = \mathbf{c}^T \mathbf{z}^{\star\star}$$
$$= \sum_{k=1}^{N} z_{k+2N}^{\star\star}$$
$$\leq \sum_{k=1}^{N} z_{k+2N}^\star$$
$$= \sum_{k=1}^{N} |x_k^\star|$$
$$= \|\mathbf{x}^\star\|_1$$
$$= m^\star.$$

Thus, we have shown

$$m^{\star\star} \leq m^\star. \tag{4.3.3}$$

On the other hand, given the minimizer $\mathbf{z}^{\star\star} \in \mathbb{R}^{3N \times 1}$ of $(P_2)$, define $\mathbf{x}^{\star\star} \in \mathbb{C}^{N \times 1}$ by

$$x_k^{\star\star} := z_k^{\star\star} + i z_{k+N}^{\star\star} \quad (k = 1, \ldots, N).$$

By construction of $\mathbf{x}^{\star\star}$, we have

$$\|A\mathbf{x}^{\star\star} - \mathbf{b}\|_2 = \|G\mathbf{z}^{\star\star} - \mathbf{h}\|_2 \leq \epsilon,$$

as obtained by expanding out the complex matrix-vector product and applying the definitions in (4.3.1). Then $\mathbf{x}^{\star\star}$ is a feasible point for $(P_1)$, so it follows that

$$
\begin{aligned}
m^{\star} &= \|\mathbf{x}^{\star}\|_1 \\
&\leq \|\mathbf{x}^{\star\star}\|_1 \\
&= \sum_{k=1}^{N} |x_k^{\star\star}| \\
&= \sum_{k=1}^{N} \sqrt{[\mathrm{Re}(x_k^{\star\star})]^2 + [\mathrm{Im}(x_k^{\star\star})]^2} \\
&= \sum_{k=1}^{N} \sqrt{[z_k^{\star\star}]^2 + [z_{k+N}^{\star\star}]^2} \\
&\leq \sum_{k=1}^{N} z_{k+2N}^{\star\star} \\
&= \mathbf{c}^T \mathbf{z}^{\star\star} \\
&= m^{\star\star}.
\end{aligned}
$$

Thus, we have shown

$$ m^{\star} \leq m^{\star\star}. \tag{4.3.4} $$

Therefore, combining (4.3.3) and (4.3.4), we have $m^{\star} = m^{\star\star}$. $\qquad\square$

Proposition 1 establishes a unique correspondence between the minimizers of $(P_1)$ and $(P_2)$. Thus, we can solve the second-order cone program $(P_2)$ instead of the complex optimization problem $(P_1)$. Apart from avoiding complex data, the SOCP $(P_2)$ has a simple linear objective function and smooth constraints.

To solve $(P_2)$, we develop an SOCP-LB solver using a standard log-barrier method. Accordingly, we define a log-barrier objective function $f_0(\mathbf{z}; \tau^q)$.

$$
\begin{aligned}
f_0(\mathbf{z}; \tau^q) = \mathbf{c}^T \mathbf{z} \quad + \quad &\frac{1}{\tau^q} \left[ \left( \sum_{k=1}^{N} -\log\left( -\frac{1}{2}\left( [z_k]^2 + [z_{k+N}]^2 - [z_{k+2N}]^2 \right) \right) \right) \right. \\
&\left. - \log\left( -\frac{1}{2}\left( \|G\mathbf{z} - \mathbf{h}\|_2^2 - \varepsilon^2 \right) \right) \right]
\end{aligned} \tag{4.3.5}
$$

where $\tau^q$ is a log-barrier parameter setting the accuracy of the approximation and $\mathbf{z}$ is the decision variable as defined in $(P_2)$

$$
\mathbf{z} := \begin{bmatrix} \mathbf{u} \\ \mathbf{v} \\ \mathbf{t} \end{bmatrix}, \text{ with } u_k := \mathrm{Re}(x_k), v_k := \mathrm{Im}(x_k), \text{ and } t_k := |x_k| \quad (k = 1, \dots, N).
$$

$$(4.3.6)$$

Since our problem does not include linear constraints as in a general SOCP , $(P_2)$ is transformed into a sequence of $q$ unconstrained programs

$$
\min_{\mathbf{z} \in \mathbb{R}^{3N}} f_0(\mathbf{z}; \tau^q), \tag{4.3.7}
$$

i.e.,

$$
\min_{\mathbf{z} \in \mathbb{R}^{3N}} \mathbf{c}^T \mathbf{z} + \frac{1}{\tau^q} \left[ \sum_{k=1}^{N} \left[ -\log \varphi_k(\mathbf{z}) \right] - \log \psi(\mathbf{z}) \right] \tag{4.3.8}
$$

where

$$
\varphi_k(\mathbf{z}) = -\frac{1}{2} \left( [z_k]^2 + [z_{k+N}]^2 - [z_{k+2N}]^2 \right), \quad (k = 1, \dots, N), \text{ or} \tag{4.3.9}
$$

$$
\varphi_k(\mathbf{z}) = -\frac{1}{2} \mathbf{z}^T H_k \mathbf{z}, \text{ and} \tag{4.3.10}
$$

$$
\psi(\mathbf{z}) = -\frac{1}{2} \left( \|G\mathbf{z} - \mathbf{h}\|_2^2 - \varepsilon^2 \right). \tag{4.3.11}
$$

The main idea of the log-barrier method is at each log-barrier iteration $q$ to solve for a series of Newton steps. The latter uses quadratic approximation $f_0(\mathbf{z} + \Delta\mathbf{z}; \tau^q)$ of the functional $f_0(\mathbf{z}; \tau^q)$ around a point $\mathbf{z}$. Therefore, the gradient $\nabla f_0(\mathbf{z}; \tau^q)$ and Hessian matrix $\mathsf{H}$ are required. For simplicity, we first set the first derivative of each of the terms in our objective function $f_0(\mathbf{z}; \tau^q)$.

$$
\frac{\partial}{\partial z_l} \left[ \mathbf{c}^T \mathbf{z} \right] = c_l, \quad (l = 1, \dots, 3N) \tag{4.3.12}
$$

$$
\frac{\partial \psi(\mathbf{z})}{\partial z_l} = -\frac{1}{2} \left[ 2(G^T G\mathbf{z})_l - 2(\mathbf{h}^T G)_l \right] \tag{4.3.13}
$$

Considering

$$H_k = \mathbf{e}_k\mathbf{e}_k^T + \mathbf{e}_{k+N}\mathbf{e}_{k+N}^T - \mathbf{e}_{k+2N}\mathbf{e}_{k+2N}^T, \quad (k = 1, \ldots, N) \tag{4.3.14}$$

and for all symmetric $B \in \mathbb{R}^{3N \times 3N}$

$$\frac{\partial}{\partial z_l}\left(\mathbf{z}^T B \mathbf{z}\right) = 2\left(B\mathbf{z}\right)_l, \tag{4.3.15}$$

$$\frac{\partial^2}{\partial z_l \partial z_m}\left(\mathbf{z}^T B \mathbf{z}\right) = 2B_{lm}, \quad (l, m = 1, \ldots, 3N), \tag{4.3.16}$$

then, the first and second order derivatives for $\varphi_k(\mathbf{z})$ are shown below

$$\frac{\partial}{\partial z_l}\left(\varphi_k(\mathbf{z})\right) = -\left(H_k\mathbf{z}\right)_l, \tag{4.3.17}$$

$$\frac{\partial^2}{\partial z_l \partial z_m}\left(\varphi_k(\mathbf{z})\right) = H_k, \quad (l, m = 1, \ldots, 3N). \tag{4.3.18}$$

Then, we define $\nabla f_0(\mathbf{z}; \tau^q)$ and $\mathsf{H}$ for problem $(P_2)$ below.

$$\begin{aligned}
\frac{\partial}{\partial z_l}\left(f_0\left(\mathbf{z}; \tau^q\right)\right) &= \frac{\partial}{\partial z_l}\left[\mathbf{c}^T z\right] + \frac{1}{\tau}\sum_{k=1}^{N}\left[-\frac{\partial}{\partial z_l}\log\varphi_k(\mathbf{z})\right] - \frac{1}{\tau}\frac{\partial}{\partial z_l}\log\psi(\mathbf{z}) \\
&= c_l - \frac{1}{\tau}\sum_{k=1}^{N}\frac{1}{\varphi_k(\mathbf{z})}\frac{\partial\varphi_k(\mathbf{z})}{\partial z_l} - \frac{1}{\tau}\frac{1}{\psi(\mathbf{z})}\frac{\partial\psi(\mathbf{z})}{\partial z_l} \\
&= c_l - \frac{1}{\tau}\sum_{k=1}^{N}\frac{\left(H_k\mathbf{z}\right)_l}{\varphi_k(\mathbf{z})} - \frac{1}{\tau}\frac{-\left(\left[G^T G\mathbf{z}\right]_l + \left(\mathbf{h}^T G\right)_l\right)}{\psi(\mathbf{z})}
\end{aligned} \tag{4.3.19}$$

As a result of the above transformations, the gradient $\nabla f_0(\mathbf{z}; \tau^q)$ of the objective function $f_0(\mathbf{z}; \tau^q)$ is expressed as

$$\nabla f_0(\mathbf{z}; \tau^q) = \mathbf{c} + \frac{1}{\tau}\left[\sum_{k=1}^{N}\frac{H_k\mathbf{z}}{\varphi_k(\mathbf{z})} + \frac{G^T G\mathbf{z} - G^T\mathbf{h}}{\psi(\mathbf{z})}\right]. \tag{4.3.20}$$

The Hessian $\mathsf{H}$ of the objective function $f_0(\mathbf{z}; \tau^q)$, respectively, is expressed as follows

$$\begin{aligned}
\nabla\nabla f_0(\mathbf{z}; \tau^q) = \frac{1}{\tau}\Bigg[&\sum_{k=1}^{N}\frac{\varphi_k(\mathbf{z})H_k - H_k\mathbf{z}\mathbf{z}^T H_k}{[\varphi_k(\mathbf{z})]^2} \\
&+ \frac{1}{[\psi(\mathbf{z})]^2}G^T[\psi(\mathbf{z})I + (G\mathbf{z} - \mathbf{h})(G\mathbf{z} - \mathbf{h})^T]G\Bigg].
\end{aligned} \tag{4.3.21}$$

Solving the linear system of equations

$$\tau \mathsf{H}\mathbf{\Delta z} \quad = \quad -\tau \nabla f_0(\mathbf{z}; \tau^q) \tag{4.3.22}$$

for $\mathbf{\Delta z} = (\mathbf{\Delta u}, \mathbf{\Delta v}, \mathbf{\Delta t})^T$, gives us the Newton step and helps proceed to find the solution of (4.3.8). The outline of the log-barrier implementation for each subproblem is given in Table 4.1.

| |
|---|
| 1. Input<br>$\quad$ $\mathbf{z}^0$ - feasible starting point<br>$\quad$ $\eta$ - tolerance<br>$\quad$ $\mu$ - parameter /a factor by which to increase the barrier constant at each iteration/<br>$\quad$ $\tau^1$ - initial log-barrier parameter /sets the accuracy of the approximation/<br>$\quad$ $k = 1$ |
| 2. Solve the optimization problem (4.3.8) with initial point $\mathbf{z}^{k-1}$<br>Call the solution $\mathbf{z}^k$ |
| 3. Terminate and return $\mathbf{z}^k$ if duality gap $\frac{m}{\tau^k} < \eta$, i.e.,<br>terminate when the solution of (4.3.8) is the same as the solution of our problem $(P_2)$.<br>(here $m$ is the number of inequality constraints) |
| 4. Else, set<br>$\quad$ $\tau^{k+1} = \mu \tau^k$<br>$\quad$ $k = k + 1$<br>and go to step 2.<br>Note that $\mu = 10 - -100$ is a reasonable choice as it results in the same number of Newton steps (around 30), required for the linear convergence of the duality gap. |

Table 4.1: An outline of log-barrier algorithm.

## 4.4 NESTA

NESTA is the second solver we choose to experiment with. It is an extension to Nesterov's algorithm [18] for compressed sensing reconstruction which can solve the quadratically constrained $\ell_1$-minimization problem $(P_1)$. Not

only can it work with complex data, but can handle nonstandard sparse reconstructions such as recovery of signals approximately sparse in a transform domain $W$. Specifically, NESTA can solve the problem

$$\min_{\mathbf{x} \in Q_p} \quad \|W\mathbf{x}\|_1$$

$$\text{subject to } \|A\mathbf{x} - \mathbf{b}\|_2 \leq \epsilon.$$

(4.4.1)

This scenario is an excellent fit to the problem $(P_1)$ we intend to solve.

The main idea in NESTA utilizing its fast execution (convergence rate $O(1/k^2)$ in the number of steps $k$) is using a first-order method for sparse recovery, i.e. a method that does not compute the Hessian matrix of the objective function as is the case in the log-barrier method. Avoiding finding the Hessian matrix is possible due to the orthogonal structure of matrix $A$, a common case in CS applications. The fact that $A$ has orthonormal rows, i.e., the product $AA^*$ is an orthogonal projector, admits fast matrix-vector product.

The outline of Nesterov's algorithm (following) demonstrates that the objective function is minimized over the primal feasible set $Q_p$, while smoothing the set, by iteratively estimating three sequences $\{\mathbf{x}_k\}$, $\{\mathbf{y}_k\}$, and $\{\mathbf{z}_k\}$. The sequence $\{\mathbf{z}_k\}$ takes into account the information of computed at previous iterations gradients to compute as an appropriate $x_k$ as possible. The two scalar sequences $\{\alpha_k\}$ and $\{\tau_k\}$ also play an important role in the algorithm.

The outline of Nesterov's algorithm is given in Table 4.2. Recall the $\ell_1$ norm is

| Initialize $\mathbf{x}^0$. For $k \geq 0$ |
| --- |
| 1. Compute $\nabla f(\mathbf{x}_k)$ |
| 2. Compute $\mathbf{y}_k$ <br> $\quad \mathbf{y}_k = \mathrm{argmin}_{\mathbf{x} \in Q_p} \frac{L_\mu}{2} \|\mathbf{x_k} - \mathbf{x}\|_2^2 + \langle \nabla f_\mu(\mathbf{x}_k), \mathbf{x} - \mathbf{x}_k \rangle$ |
| 3. Compute $\mathbf{z}_k$ <br> $\quad \mathbf{z}_k = \mathrm{argmin}_{\mathbf{x} \in Q_p} \frac{L_\mu}{2} \|\mathbf{x} - \mathbf{x}_0\|_2^2 + \langle \sum_{i \leq k} \alpha_i \nabla f_\mu(\mathbf{x}_k), \mathbf{x} - \mathbf{x}_k \rangle$ |
| 4. Update $\mathbf{x}_k$ <br> $\quad \mathbf{x}_k = \tau_k \mathbf{z}_k + (1 - \tau_k)\mathbf{y}_k$ |
| Terminate when a selected criterion is valid. |

Table 4.2: An outline of Nesterov's algorithm

of the form Nesterov's algorithm assumes the objective function is differentiable
and its gradient $\nabla f(\mathbf{x})$ is Lipschitz obeying

$$\|\nabla f(\mathbf{x}) - \nabla f(\mathbf{y})\|_2 \leq L \|\mathbf{x} - \mathbf{y}\|_2 \tag{4.4.2}$$

with $L$ an upper bound on the Lipschitz constant. To guarantee the smooth-
ness of the $\ell_1$ norm being the objective function in our problem (4.4.1), the
method approximates it with the Huber function $f_\mu$

$$f_\mu = \max_{\mathbf{x} \in Q_p} \langle \mathbf{u}, W^* \mathbf{x} \rangle - \frac{\mu}{2} \|\mathbf{u}\|_2^2 \tag{4.4.3}$$

Thus, the algorithm solves an equivalent to (4.4.1) problem, the smooth con-
strained problem

$$\min_{\mathbf{x} \in Q_p} \quad f_\mu(\mathbf{x}) \tag{4.4.4}$$

where $Q_p = \{\mathbf{x} : \|A\mathbf{x} - \mathbf{b}\|_2 \leq \epsilon\}$.

The gradient is equal to

$$\nabla f_\mu(\mathbf{x}) = W \mathbf{u}_\mu(\mathbf{x}) \tag{4.4.5}$$

with $\mathbf{u}_\mu(\mathbf{x})$ of the form

$$\mathbf{u}_\mu(\mathbf{x})[i] = \begin{cases} \mu^{-1}(W^*\mathbf{x}[i]), & \text{if } |(W^*\mathbf{x})[i]| < \mu, \\ sgn((W^*\mathbf{x})[i]), & \text{otherwise.} \end{cases} \tag{4.4.6}$$

NESTA as introduced in [16] appears to be an accurate, computationally effi-
cient approach with the great advantage of robust excellent performance not
dependent on tuning too many parameters. In practice, we only tune $\mu$, the
smoothing parameter.

# Chapter 5

# Results

## 5.1 Experimental Protocol

The experiments which we set aim to compare the SOCP solver with log-barrier method (referred to as SOCP-LB solver) and the NESTA solver for sparse recovery with Lustig's solver using Non-linear Conjugate Gradient (NLCG) method (referred to as NLCG solver). To achieve this goal, two major difficulties related to the equivalence in the different formulations of the optimization problem solved need to be overcome.

Lustig solves the problem in its Lagrangian form as defined in (4.2.3) while SOCP-LB and NESTA methods solve the quadratically constrained $\ell_1$-minimization problem (4.2.1). Each formulation uses either $\epsilon$ or $\lambda$. Therefore, we need to determine a relation between these two parameters which will ensure equivalence between the problems of interest, i.e., we need to find $\epsilon(\lambda)$ or $\lambda(\epsilon)$. $\lambda$ can be found theoretically by writing the Karush-Kuhn-Tucker (KKT) conditions of the system (for a reference on KKT see [13, 15]). Since in practice we find the approximate solution of the system, using this strategy to compute $\lambda$ is unstable. Hence, it is difficult to find $\lambda(\epsilon)$ for a given $\epsilon$ [16].

As a substitute, we adopt a procedure similar to the one described in [16]: we

fix $\lambda$ in the NLCG solver to find solution $\mathbf{x}_\lambda$, used as a benchmark solution, and then find $\epsilon(\lambda)$. Since $\epsilon = \|A\mathbf{x} - \mathbf{b}\|_2$, we substitute with the so found $\mathbf{x}_\lambda$ and obtain a value of $\epsilon$ corresponding to the fixed $\lambda$. Thus, the pair $(\lambda, \epsilon)$ provides nearly equivalent solutions of the SOCP-LB, NESTA, and NLCG algorithms. The solution of the Lagrangian algorithm implemented in the NLCG solver will be used to judge the accuracy of the tested algorithms.

The second major difficulty is the difference in the stopping criteria of each algorithm. To make these directly comparable, a new terminating criterion (as [16] suggests, a fair one) replaces the originally implemented stopping criteria. Namely, given NLCG's solution $\mathbf{x}_\lambda$, the other algorithms terminate when the solution $\widehat{\mathbf{x}_k}$ at iteration $k$ is as accurate as $\mathbf{x}_\lambda$

$$\|\widehat{\mathbf{x}_k}\|_1 \leq \|\mathbf{x}_\lambda\|_1 \quad \text{and} \quad \|A\widehat{\mathbf{x}_k} - \mathbf{b}\|_2 \leq 1.05\|A\mathbf{x}_\lambda - \mathbf{b}\|_2 \tag{5.1.1}$$

Since both methods, the SOCP-LB and NESTA, solve (4.2.1) formulation of the problem, we implement and run the tests with only this as opposed to two criteria in [16]. Moreover, the claim of the authors of [16] is that the results of applying the two criteria do not differ significantly.

## 5.2   Numerical Results

The series of experiments we run test the performance of both the SOCP-LB and NESTA solver on a brain image. The brain image is encoded by a fast spin-echo (FSE) pulse sequence [1], thus, obtaining the complete set of its Fourier coefficients. By inverse Fourier transform, we compute the coefficients of the brain image in its image domain. Those coefficients are utilized later in finding the errors in the reconstructed images. To run the experiments, vector $\mathbf{b}$, which is the vector of the undersampled Fourier coefficients, has been constructed the following way. We take the original image and by applying the Monte-Carlo incoherent sampling scheme (Section 3.5) to the fully encoded brain image

obtain the undersampled Fourier coefficients. In our experiments here, $N = 2621414$, $M = 102912$, and $K = 19389$. The acceleration factor is 2.4. In this situation, the recovery is performed with the same wavelets (Daubechies,4,4) and different fixed values of $\mu$ (duality gap or smoothing parameter) and $\epsilon(\lambda)$ ($\ell_2$ constraint parameter) as described in Table 5.1. The three columns in this table report respectively: the standard deviation of the clock time $t(sec)$ (the time for computing the solution) over 5 trials; the absolute error of each solution compared to the original fully sampled image

$$er_{abs} = \|\mathbf{x}_{original} - \mathbf{x}_{approximated}\|_2; \tag{5.2.1}$$

and last, the absolute error of each of the solvers (the SOCP-LB and NESTA) compared to our benchmark - the NLCG solution,

$$Error = \|\mathbf{x}_{benchmark} - \mathbf{x}_{approximated}\|_2; \tag{5.2.2}$$

The initial guess $\widehat{\mathbf{x}}_0$ is set the same for all three algorithms as $A\widehat{\mathbf{x}}_0 = \mathbf{b}$. All experiments are run on a machine Intel(R) Corel(TM)2 Duo CPU P8600 @ 2.40GHz, 2.39GHz, 2.99 GB of RAM.

Figures (5.2 - 5.3) depict the CS reconstructions of the exact brain image (Figure 5.1a) with the above mentioned solvers. The numbers in Table 5.1 dictate that regardless of the values of $\mu$ (duality gap or smoothing parameter) the fastest, $t \sim 3.8$sec, and most robust in terms of the preserving same small $er_{abs} \sim 4.8$ is the SOCP-LB solver. The NLCG solver performs nearly 5 times slower but with $er_{abs} \sim 5.9$ comparable to the SOCP-LB solver $er_{abs}$ for all tested values of $\mu$. While NESTA performs nearly as fast as the SOCP-LB solver (its time is $t \sim 4.1 - 5.9$sec for all $\mu$), it achieves excellent performance for small $\mu = 1e-15$ with its $er_{abs} \sim 5.5$ close to the $er_{abs}$ of the NLCG solver. With increasing the value of $\mu$, NESTA's performance significantly drops; its $er_{abs}$ reaches 43.923 for $\mu = 1e-6$ (see Figure 5.4). This respectively influences its *Error* which also grows with the growth of the duality gap. $er_{abs}$ (for NLCG, SOCP-LB, and NESTA) and *Error* (for SOCP-LB and NESTA) are imaged on Figure 5.5 and Figure 5.6, respectively.

Figure 5.7 displays (a) the magnitudes of the unsorted wavelet coefficients of the approximated solutions and (b) the respective absolute error computed as a difference from the wavelet coefficients of the exact image. The figure demonstrates that all reconstructions are pretty close to the original image for $\mu = 1e - 15$. The figure is also supports the results as shown in Table 5.1 and as commented above.

Similar results are observed in the cases when we choose 1) different fixed $\epsilon(\lambda)$ (shown in Table 5.2) for the different values of $\mu$ as used in the series of experiments with $\lambda = 0.005$ and 2) a different image to reconstruct (images used are noisy phantom (Figure 5.1b) and breast phantom (Figure 5.1c )).

| | | $\lambda = 0.005,$ | $\epsilon(\lambda) = 0.2436$ | |
|---|---|---|---|---|
| $\mu$ | Method | $t(sec)$ | $er_{abs}$ | $Error$ |
| 1e-15 | NLCG | 15.327587 | 5.9597 | na |
| | SOCP-LB | 3.7845364 | 4.7928 | 6.3019 |
| | NESTA | 4.1371854 | 5.5377 | 6.5961 |
| $\mu$ | Method | $t(sec)$ | $er_{abs}$ | $Error$ |
| 1e-10 | NLCG | 15.3338892 | 5.9595 | na |
| | SOCP-LB | 3.7508208 | 4.7928 | 6.3018 |
| | NESTA | 5.9046468 | 31.1794 | 31.2693 |
| $\mu$ | Method | $t(sec)$ | $er_{abs}$ | $Error$ |
| 1e-6 | NLCG | 15.2934796 | 5.7067 | na |
| | SOCP-LB | 3.796163 | 4.7928 | 6.0604 |
| | NESTA | 4.735928 | 43.9234 | 43.9228 |

Table 5.1: Recovery results of brain image, size [512, 512], N = 262 144, M = 102 912, K = 19389 /$\mu$ - smoothing parameter or duality gap, $\epsilon(\lambda)$ - $l_2$ constraint parameter chosen to a corresponding $\lambda$/.

| $\lambda$ | $\epsilon(\lambda)$ | $\sigma$ |
|---|---|---|
| 0.05 | 1.136 | 3.5e-3 |
| 0.005 | 0.2436 | 9.1455e-4 |
| 0.00005 | 0.1276 | 3.9654e-4 |

Table 5.2: Corresponding values of $\lambda$, $\epsilon(\lambda)$, and $\sigma$(noise level) used in the experiments.
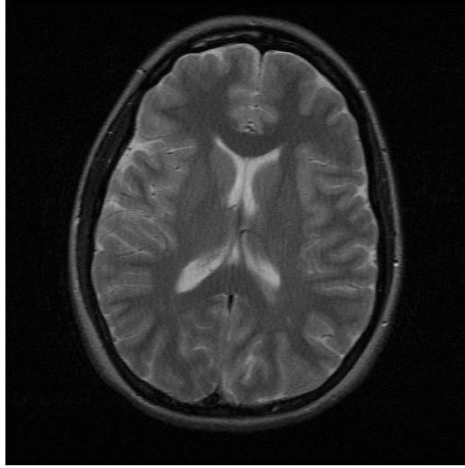
(a) Brain image
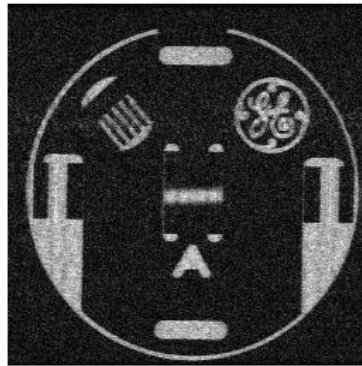


(b) Noisy phantom
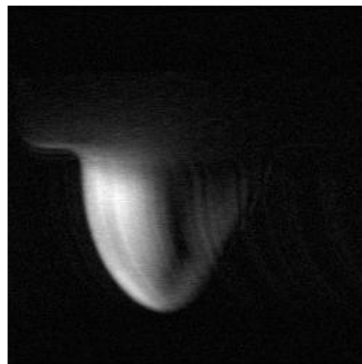


(c) Breast phantom

Figure 5.1: Images used in the experiments.
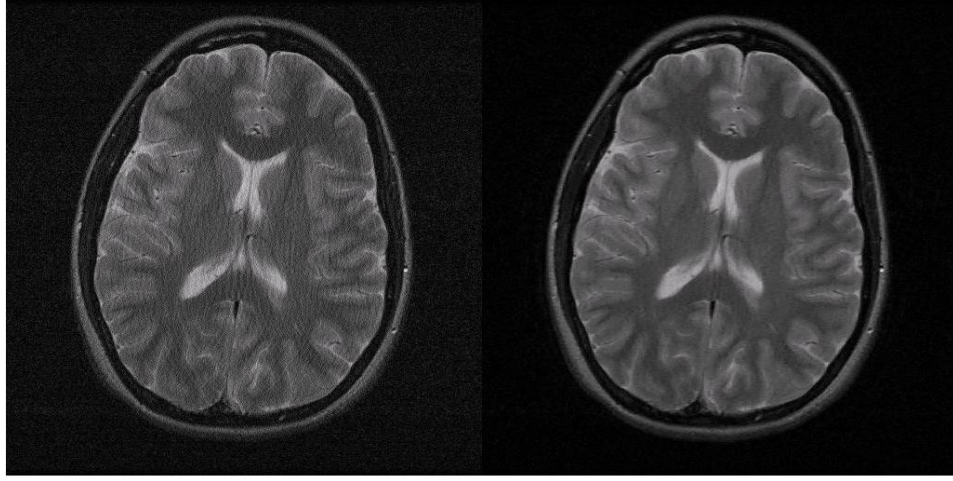
(a) NLCG
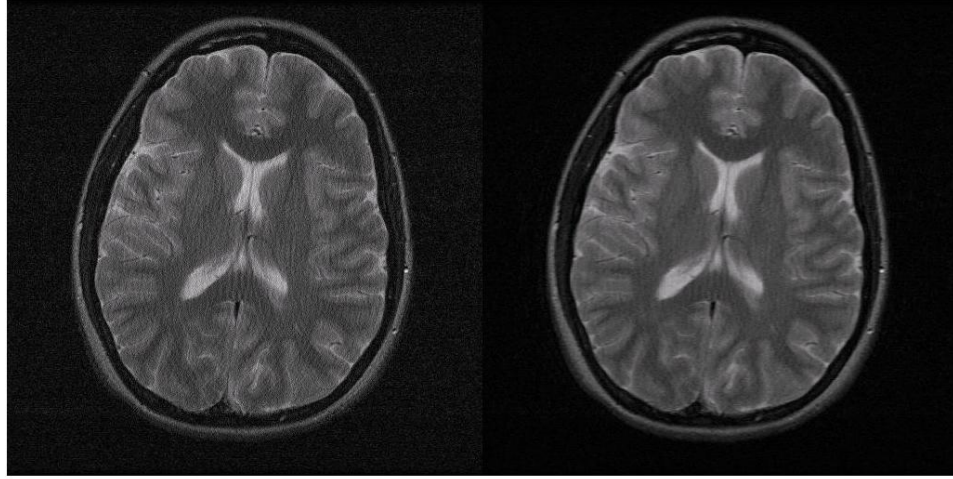

(b) SOCP-LB
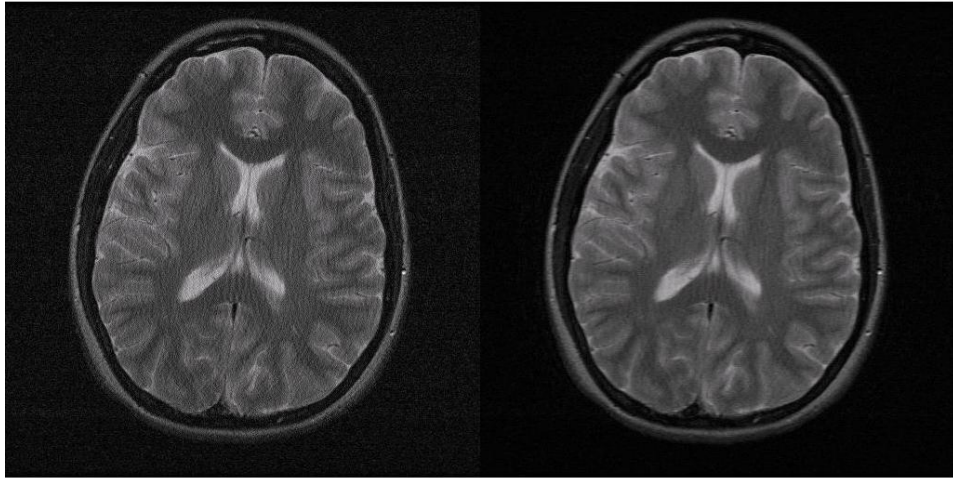

(c) NESTA

Figure 5.2: Initial guess of the reconstruction (left), Approximation of the brain image (right), $/\lambda = 0.005$, $\epsilon(\lambda) = 0.2436$, $\mu = 1e - 15/$.
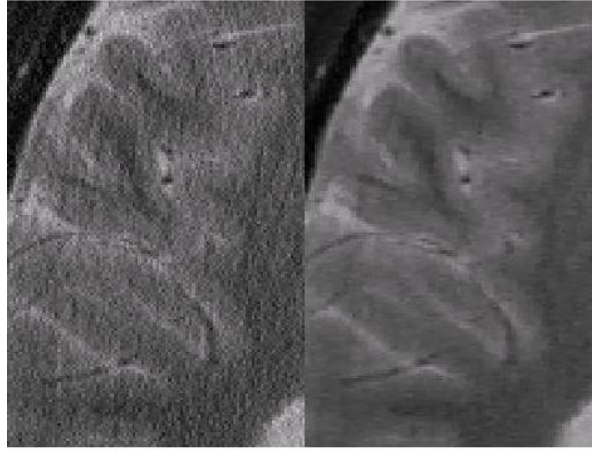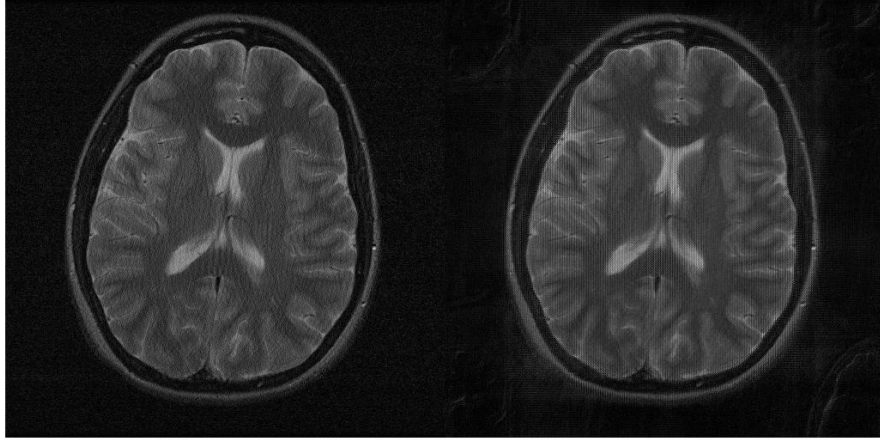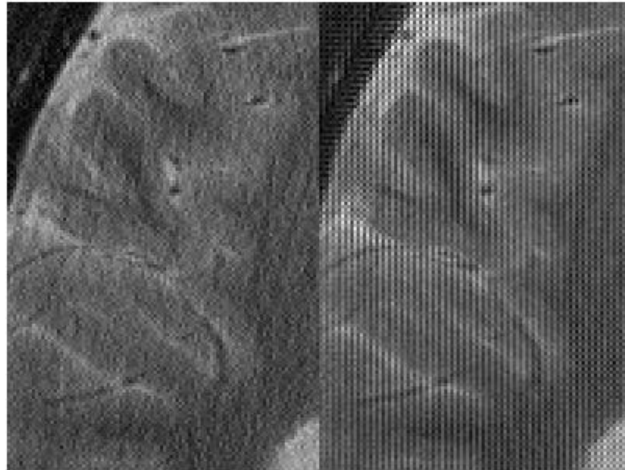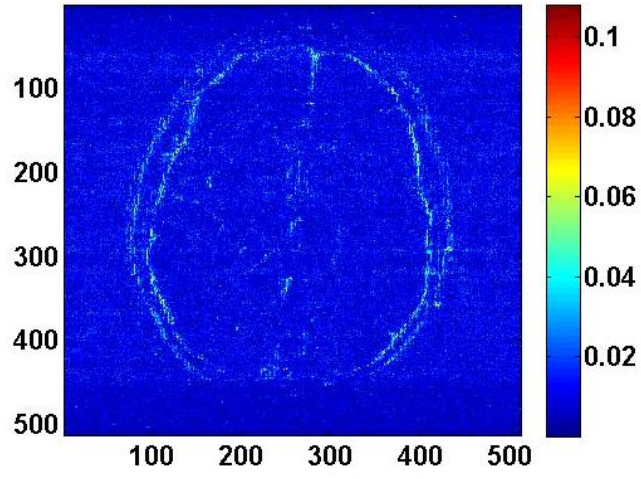
(a) NLCG
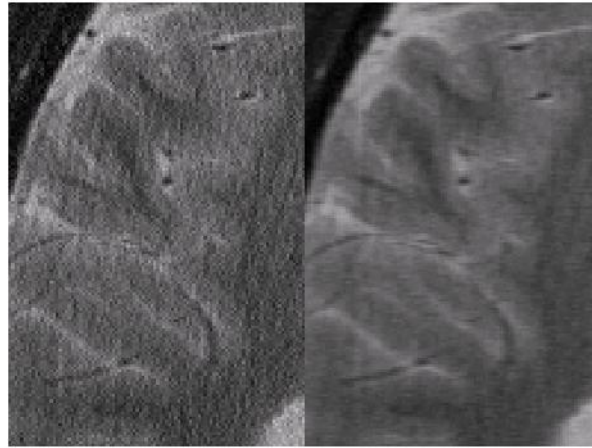

(b) SOCP-LB


(c) NESTA

Figure 5.3: Initial guess of the reconstruction (left), Approximation of the brain image (right) (zoom in), $/\lambda = 0.005$, $\epsilon(\lambda) = 0.2436$, $\mu = 1e - 15/$.

(a) Initial guess of the reconstruction (left), Approximation of the brain image (right)



(b) Initial guess of the reconstruction (left), Approximation of the brain image (right)(zoom in)

Figure 5.4: NESTA's performance at $/\lambda = 0.005$, $\epsilon(\lambda) = 0.2436$, $\mu = 1e - 6/$.
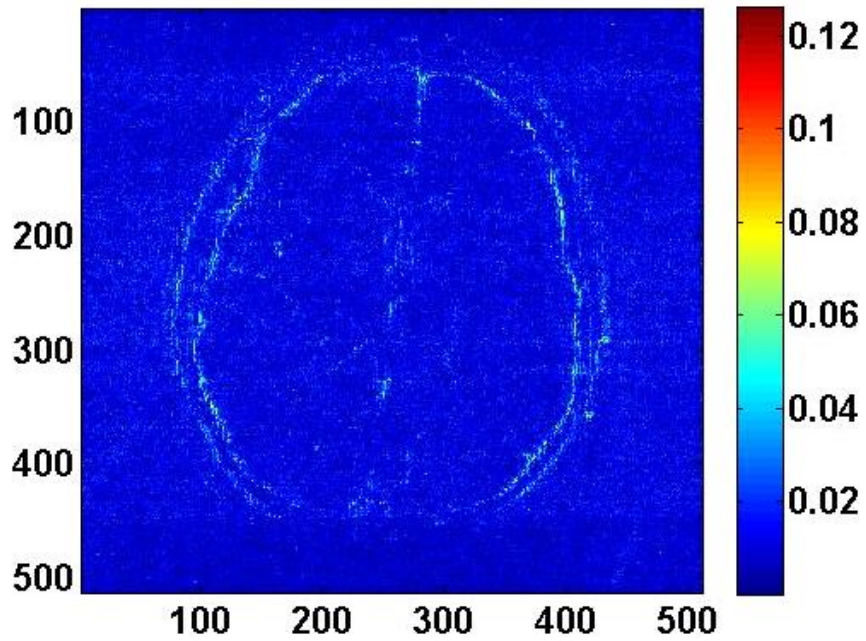
(a) NLCG
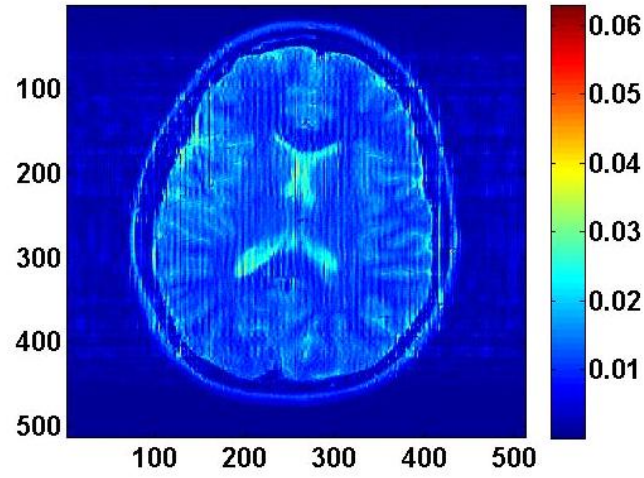


(b) SOCP-LB
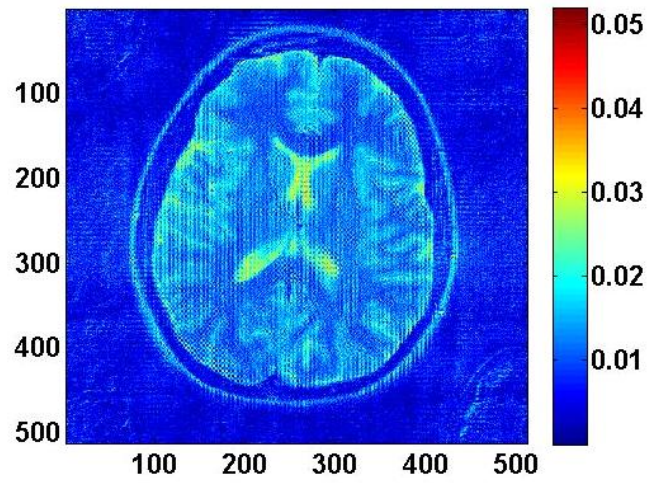


(c) NESTA

Figure 5.5: $er_{abs}$ for the three solvers, $/\lambda = 0.005$, $\epsilon(\lambda) = 0.2436$, $\mu = 1e-15/$.
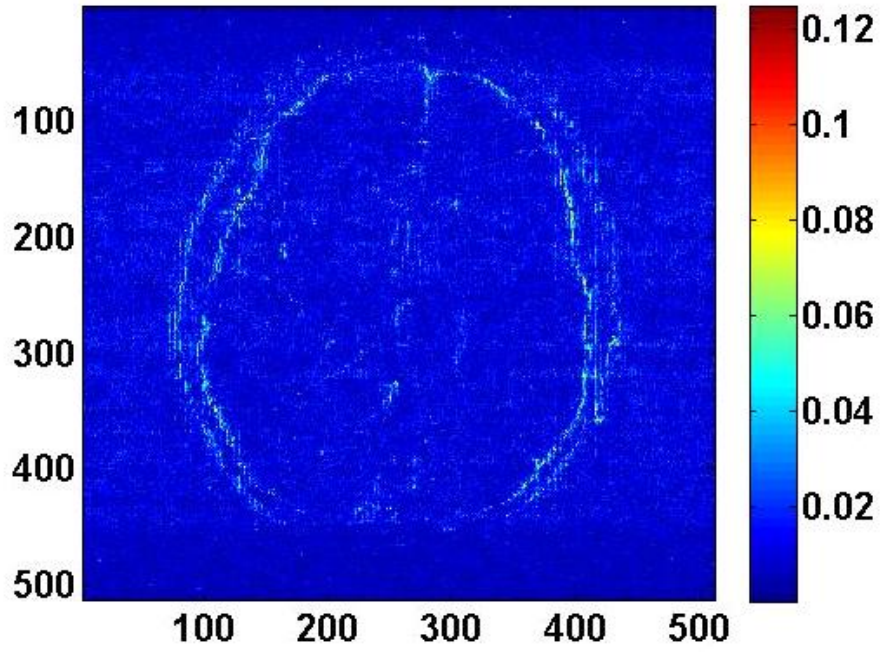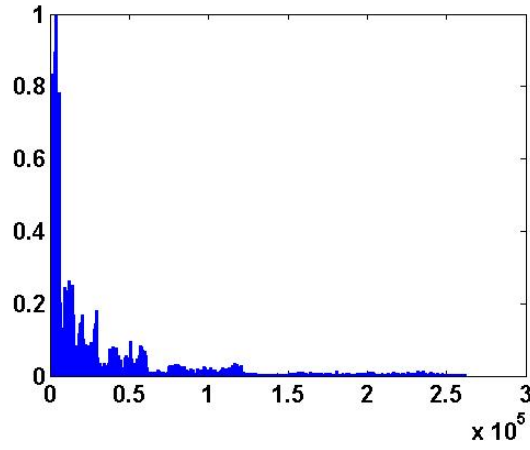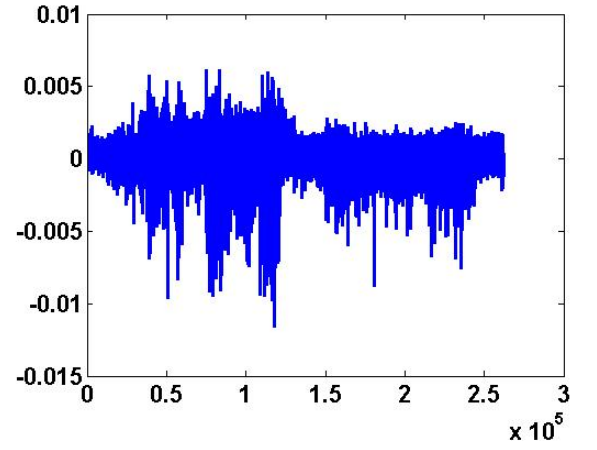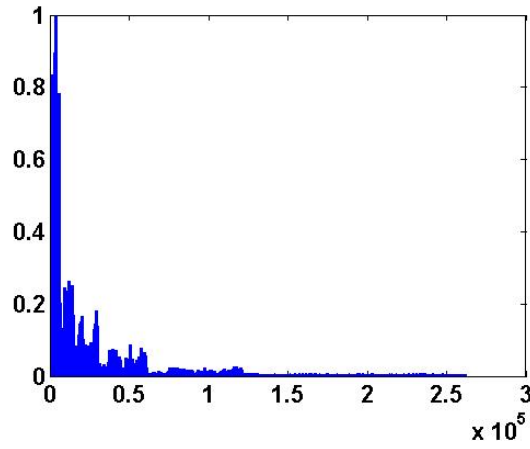
(a) SOCP-LB



(b) NESTA

Figure 5.6: The absolute error *Error* for the SOCP-LB and NESTA solutions compared to the benchmark solution NLCG, $/\lambda = 0.005$, $\epsilon(\lambda) = 0.2436$, $\mu = 1e - 15/$.
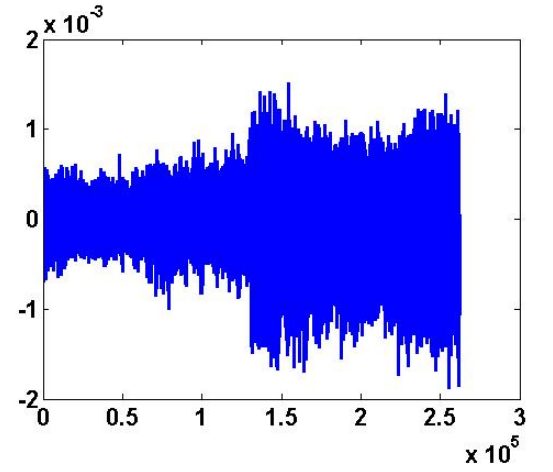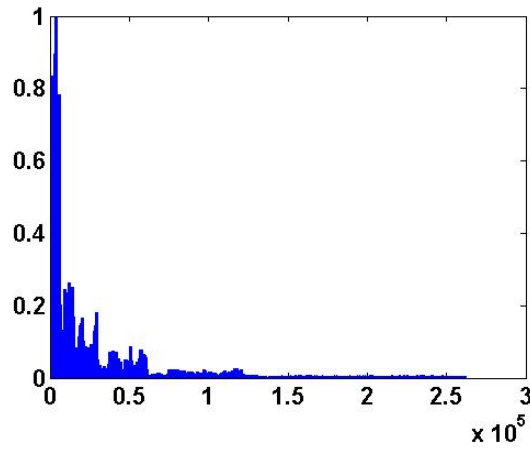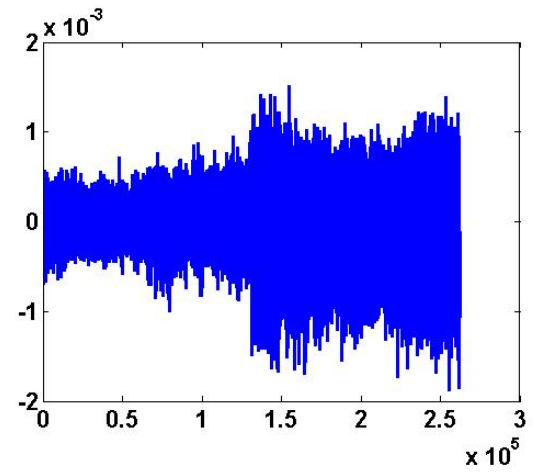
(a) NLCG

(b) NLCG

(c) SOCP-LB

(d) SOCP-LB

(e) NESTA

(f) NESTA

Figure 5.7: Unsorted wavelet coefficients for the three solvers (left column), Unsorted wavelet coefficients absolute error for the three solvers (right column), $/\lambda = 0.005$, $\epsilon(\lambda) = 0.2436$, $\mu = 1e - 15/$.

# Chapter 6

# Conclusion and Future Work

Two different methods of a sparse image reconstruction solving the SOCP formulation of the convex optimization problem have been studied: the SOCP-LB solver and NESTA. It has been shown that both algorithms are accurate and competitive with the NLCG solver, our benchmark algorithm, under tuning the corresponding parameters.

We have specifically developed the SOCP-LB solver, implementing the log-barrier method (as described in [13] and used in [17] for recovering real sparse signals), in such a way that complex input data can be handled directly. Since the sparse structure of the Hessian matrix is accounted for, which for larger scale problems (as ours, $512 \times 512$ matrices) is complemented by the matrix-free approach, the SOCP-LB solver performs fast. In fact, of all three MRI sparse applications tested, the SOCP-LB solver outperforms the other solvers - slightly faster than NESTA and three times faster than the benchmark NLCG. Moreover, the SOCP-LB's error is robust to varying the duality gap and $l_2$ constraint parameter. This result is of great significance as it achieves the goal of reducing the processing time of a sparse MR image reconstruction without compromising the image quality.

In the SOCP-LB solver the general formulation of the quadratically con-

strained optimization problem for complex variables has been redefined in terms of real variables. This redefinition has not been explicitly shown in the convex optimization literature before. Therefore, we provide a proof for the equivalence of the complex optimization problem and the second order cone program. The importance of this redefinition is that it can easily be implemented in any SOCP solver (commercial or publicly released) requiring real input.

It has been found that the results from NESTA, a solver based on a first-order method for sparse recovery, follow closely the results from the SOCP-LB solver, provided the smoothing parameter is set to its lowest allowed value. These are other important results as they confirm NESTA serves as a reliable publicly released tool for solving compressed sensing MRI recovery problems, under the condition mentioned above. Moreover, NESTA is convenient to use since it depends neither on the type of input (real or complex) nor on tuning too many parameters.

Many other algorithms (cited in [16]) perform with comparable to the SOCP-LB and NESTA accuracy and speed. These two algorithms, however, have a number of advantages. They can deal equally well with sparse as well as with approximately sparse images (which is most commonly the case in medical imaging). They are also extremely flexible in the sense that the efficiency of the algorithm is reached by tuning a small number of parameters. Finally, they solve a more practical formulation of the sparse signal reconstruction problem. Practicality is related to the SOCP formulation of solving the convex optimization problem. More specifically, this formulation depends on the noise constraint parameter. The noise constraint parameter, on the other hand, is more natural to determine compared to Lagrangian parameter (the parameter required in solving the Lagrangian formulation of the convex problem). These advantages can turn them into preferred tools for compressed sensing magnetic resonance imaging reconstructions.

Future work can expand the study of solving the SOCP problem directly for more MRI applications, not limited to the algorithms reviewed in this thesis. There is also a possibility of developing special implementations of SOCP solvers for this specific application. This can include preconditioning the linear systems solved within the Newton steps by exploiting the structure of the Hessian. Further, improved incoherent transform domains tailored to the sampling operator as well as optimal sampling trajectories can be developed and tailored to specific MR images with the hope of even better performance. Improvements in any of these directions will be of benefit to the clinical MRI diagnosis and in particular to reducing the cost of MRI.

# Bibliography

[1] Z. P. Liang , P. C. Lauterber. *Principles of Magnetic Resonance Imaging: A Signal Processing Perspective.* Wiley-IEEE Press, 1999.

[2] M. Lustig. *Sparse MRI* . PhD Thesis, Stanford University, August 2008.

[3] M. Lustig, D. Donoho, J. M. and Pauly. Sparse MRI: The Application of Compressed Sensing for Rapid MR Imaging. *Magnetic Resonance in Medicine*, 58:1182–1195, 2007.

[4] M. Lustig, D. Donoho, J. M. Santos, and J.M. Pauly. Compressed Sensing MRI. *IEEE Signal Processing Magazine*, 58:1182–1195, 2007.

[5] R. G. Baraniuk. Compressive Sensing. *IEEE Signal Processing Magazine*, 24:1053–5888, 2007.

[6] J. Romberg. Imaging via Compressive Samping. *IEEE Signal Processing Magazine*, 24:1053–5888, 2007.

[7] E. Candes, M. Wakin. An introduction to compressive sampling. *IEEE Signal Processing Magazine*, 25, 2008.

[8] E. Candes, J. Romberg, and T. Tao. Robust Uncertainty Principles: Exact Signal Reconstruction from Highly Incomplete Frequency Information. *IEEE Trans. Inform. Theory*, 52(2):489–509, Feb. 2006.

[9] D. A. Koff, H. Shulman. An Overview of Digital Compression of Medical Images: Can We Use Lossy Compression in Radiology?. *CARJ*, 4:211–217, 2006.

[10] J-L. Starck, M. Elad, and D. L. Donoho. Image decomposition via the combination of sparse representations and a variational approach. *IEEE Trans. On Image Processing*, 14(10):1570–1582, 2005.

[11] D. S. Taubman, M. W. Marcellin. *JPEG 2000: Image Compression Fundamentals, Standards and Practice.* Kluwer International Series in Engineering and Computer Science., 2002.

[12] R. G. Baraniuk, J. Romberg, M. Wakin. *Tutorial on Compressive Sensing.* Seminar Talk, University of Michigan, February, 2008.

[13] S. Boyd, L. Vandenberghe. *Convex Optimization.* Cambridge University Press, 2004.

[14] M. S. Lobo, L. Vandenberghe, S. Boyd, H. Lebret. Applications of Second-order Cone Programming. *Linear Algebra and its Applications*, 284:193–228, 1998.

[15] J. Nocedal, S. J. Wright. *Numerical Optimization.* Springer-New York, 1999.

[16] S. Becker, J. Bobin, E. Candes. *NESTA: A fast and Accurate First-order Method for Sparse Recovery.* Technical Report, California Institute of Technology, April 2009.

[17] E. Candes, J. Romberg. $\ell_1$-*magic : Recovery of Sparse Signals via Convex Programming.* User's Guide , Caltech, October 2005.

[18] Y. Nesterov. *A method for unconstrained convex minimization problem with the rate of convergence $O(1 / k^2)$.* Doklady AN USSR (translated as Soviet Math. Docl.), 269, 1983.

[19] T. G. Feeman. *The Mathematics of Medical Imaging, A Beginners Guide.* Springer-New York, 2010.

[20] S. S. Chen, D. L. Donoho, and M. A. Saunders. Atomic decomposition by basis pursuit. *SIAM J. Scientific Computing*, 20:33-61, 1999.

[21] M. Blaimer, F. Breuer, M. Mueller, R. M. Heidemann, M. A. Griswold, and P. M. Jakob. SMASH, SENSE, PILS, GRAPPA-How to Choose the Optimal Method. *Top Magn Reson Imaging*, 15:223-236, 2004.

[22] J. J. van Valls, M. E. Brumrner, W. T. Dixon, H. H. Tuithof, H. Engels, R. C. Nelson, B. M. Gerety, J. L. Chezmar, and J. A. Boer. Keyhole method for accelerating imaging of contrast agent uptake. *J Magn Reson Imaging*, 3:671–675, 1993.

[23] Michael Joy. *Medical Imaging Course.* Lectures, University of Toronto, 2009.

[24] D. Donoho, Y. Tsaig, I. Drori, and J.-L. Starck. *Sparse solution of underdetermined linear equations by stagewise orthogonal matching pursuit.* Technical Report, Department of Statistics, Stanford University, 2006, preprint.

[25] K. T. Block, M. Uecker, and J. Frahm. Undersampled radial MRI with multiple coils. Iterative image reconstruction using a total variation constraint. *Magn Reson Med*, 57(6):1086-1098, Jun 2007.

[26] K. K. Herrity, A. C. Gilbert, and J. A. Tropp. Sparse approximation via iterative thresholding. *Proc. ICASSP*, 3:624–627, Toulouse, May 2006.

[27] D. Donoho. For most large underdetermined systems of linear equations, the minimal '1 solution is also the sparsest solution. *Comm. Pure Appl. Math.*, 59:797-829, June 2006.

[28] A. Feuer, and A. Nemirovsky. On sparse representations in pairs of bases. *IEEE Transactions on Information Theory*, 49:1579-1581, 2003.

[29] R. Gribonval, and M. Nielsen. Sparse representations in unions of bases. *IEEE Transactions on Information Theory*, 49:3320–3325, 2003.